The Shape of Dark Matter Haloes: Results from Weak Lensing

by

Bailey Robison

A thesis
presented to the University of Waterloo
in fulfillment of the
thesis requirement for the degree of
Master of Science
in
Physics

Waterloo, Ontario, Canada, 2020

Author's Declaration

This thesis consists of material all of which I authored or co-authored: see Statement of Contributions included in the thesis. This is a true copy of the thesis, including any required final revisions, as accepted by my examiners.

I understand that my thesis may be made electronically available to the public.

Statement of Contributions

The derivation of $n(z)$ by re-weighting a spectroscopic sample was performed by Isaac Spitzer.

Shape measurements of source galaxies were generated using ShapePipe, a shape measurement pipline developed by Guinot A., Farrens S., Kilbinger M. et al. at the Centre d'Energie Atomique (CEA)/Université Paris-Saclay.

The majority of the content presented in this thesis is my own work.

Abstract

Dark matter haloes are expected to have a triaxial shape, appearing elliptical in projection. Understanding the orientation of these dark matter haloes, and how they are aligned, has implications for theories of structure formation in the universe. Additionally, a better understanding of halo alignment will allow us to account for intrinsic alignments and improve future weak lensing studies. We measure dark matter halo ellipticity using weak galaxy-galaxy lensing. We study the anisotropic shear around luminous red galaxies (LRGs) from the Baryon Oscillation Spectroscopic Survey (BOSS), using galaxies from the Canada-France Imaging Survey (CFIS) as background source galaxies. By aligning with the major axis of the galaxy light before measuring the shear, we can stack many lens galaxies to obtain a detection of halo ellipticity. We model the dark matter mass distribution as a multipole expansion, with an isotropic monopole component and a quadrupole that accounts for the angular dependence and ellipticity. We calculate 6 quadrupole estimators, which are designed to measure anisotropic lensing signal while minimising any isotropic contributions. Taking the results from these estimators into account, we obtain a mean halo ellipticity of $e = 0.226 \pm 0.102$. We also study the lensing signal when aligning with filaments, using pairs of LRGs as a proxy. This also yields a detection of dark matter anisotropy. A meaningful measure of ellipticity along the filaments will require further development of the model to account for anisotropy on larger scales.

Acknowledgements

Table of Contents

List of Figures

List of Abbreviations

BOSS Baryon Oscillation Spectroscopic Survey 12

CFHTLenS Canada-France-Hawaii Lensing Survey 11

CFIS Canada-France Imaging Survey 8

CJ Clampitt-Jain 31

DM dark matter 1

FFT fast Fourier transform 74

LRG luminous red galaxy 7

NFW Navarro-Frenk-White 6

NR Natarajan-Refregier 35

SDSS Sloan Digital Sky Survey 7

List of Symbols

c_{200} Concentration. How the scale radius of the NFW profile is related to the virial radius. 28

$\Delta\Sigma_1^{(+)}$ Positive γ_1 Clampitt-Jain estimator. This estimator measures γ_1 in the region where $\cos(4\theta)$ is positive. 32

$\Delta\Sigma_1^{(-)}$ Negative γ_1 Clampitt-Jain estimator. This estimator measures γ_1 in the region where $\cos(4\theta)$ is negative. 32

$\Delta\Sigma_2^{(+)}$ Positive γ_2 Clampitt-Jain estimator. This estimator measures γ_2 in the region where $\sin(4\theta)$ is positive. 33

$\Delta\Sigma_2^{(-)}$ Negative γ_2 Clampitt-Jain estimator. This estimator measures γ_2 in the region where $\sin(4\theta)$ is negative. 33

$\Delta\Sigma(R)$ Excess projected surface mass density. This is directly related to the observed shear. It is a measure of how much more mass is contained within a certain radius than at that radius. 5

e_1 First ellipticity coordinate. This coordinate describes the shape of an image in the vertical or horizontal direction. 4

e_2 Second ellipticity coordinate. This coordinate describes the shape of an image in either of the diagonal directions. 4

e Ellipticity of the dark matter halo. This depends on the semi-major and semi-minor axes, $e = (a - b)/(a + b)$. Rounder haloes will have a lower ellipticity, while more elongated haloes will have a higher ellipticity. 6

$f_{45}\Delta\Sigma$ Cross shear Mandelbaum estimator. This estimator weights the cross shear of each source by $\sin(2\theta)$ when stacking. 35

$f\Delta\Sigma$ Tangential shear Mandelbaum estimator. This estimator weights the tangential shear of each source by $\cos(2\theta)$ when stacking. 35

γ Shear. The amount a background image is stretched by a foreground mass distribution. This is related to the excess mass distribution. 3

κ Convergence. The amount an image is resized isotropically. This is related to the projected mass distribution. 3

M_{200} Virial mass. A measure of the mass of a dark matter halo. The mass contained within the virial radius assuming a spherical volume. 28

R_{200} Virial radius. A measure of the size of a dark matter halo. The radius within which the average density is 200 times the critical density. 28

Σ_{crit} Critical density. This is used to relate observed shear to projected mass distribution. Depends on the distances to the source and the lens. 5

Chapter 1

Introduction

In the standard ΛCDM cosmological model of our universe, dark matter (DM) accounts for over 80% of the matter content. This dark matter plays a dominant role in the formation and evolution of large scale structure in the universe. Dark matter haloes, in which galaxies reside, assemble in a hierarchical manner, with less massive haloes accreting into more massive ones. Simulations have revealed that filaments and other forms of large scale structure will have an effect on the rate and direction of the accretion of smaller haloes (van Haarlem & van de Weygaert, 1993). This will lead to triaxial dark matter haloes that appear elliptical in projection, which have been observed in simulations (Dubinski & Carlberg, 1991; Jing & Suto, 2002). The orientation of these haloes will be highly dependent upon the surrounding large scale structure (Aragón-Calvo et al., 2007). Developing a more comprehensive understanding of dark matter halo ellipticity, and how their alignments depend on their environment, will have implications for theories of structure formation.

The anisotropy of dark matter haloes has implications for many fields of study. We are primarily interested in the implications dark matter anisotropy has on the field of weak lensing. Weak lensing is a powerful tool that can be used to observe matter on large scales, but measurements require an understanding of a variety of systematic effects. In weak lensing, an assumption is made that all sources are oriented randomly and therefore any coherent alignment is due to lensing. In reality, galaxies will have some intrinsic alignment due to gravitational interaction with surrounding structure and galaxies. This intrinsic alignment is a significant source of contamination in weak lensing.

In weak lensing, one must average across pairs of observed galaxy shapes (γ^{obs}). This shape depends on both the intrinsic ellipticity (γ^I) and the distortion due to lensing (γ^G).

The ellipticity correlation function is

$$\langle \gamma^{obs} \gamma^{obs} \rangle = \langle \gamma^G \gamma^G \rangle + \langle \gamma^I \gamma^G \rangle + \langle \gamma^G \gamma^I \rangle + \langle \gamma^I \gamma^I \rangle \tag{1.1}$$

The first term is the shear signal (GG) with which we are primarily concerned. However, coherent intrinsic alignments can cause the middle two terms (GI) and the final term (II) to become significant contaminants. The weak lensing signal only accounts for a small part of the observed source shape, with γ^G accounting for roughly 1% of the observed shape (Hirata & Seljak, 2004). As a result, small contributions from intrinsic alignments can completely erase any weak lensing signal. These GI and II contamination effects have been previously observed (Mandelbaum et al., 2006a; Hirata et al., 2007; Okumura & Jing, 2009).

Contamination from the GI term can be on the order of 10% for a typical weak lensing survey (Hirata et al., 2007). If this contamination is unaccounted for, it can lead to significant bias in measurements of cosmological parameters. The parameter σ_8 measures matter fluctuations on the scale of 8 Mpc/h and describes the growth of structure in the universe. Weak lensing can be used to observe the matter power spectrum, from which σ_8 is derived. Contamination from intrinsic alignments could cause σ_8 to be underestimated by as much as $\sim 10\%$ (Schneider & Bridle, 2010). Improving our model of halo anisotropy will allow us to study and develop a better understanding of these intrinsic alignments. Once these intrinsic alignments can be accounted for, results for future weak lensing studies can be improved.

Another benefit of measuring dark matter halo ellipticity is that it provides another test for modified theories of gravity. These theories eschew dark matter and attempt to explain phenomena attributed to dark matter with only baryonic matter. Modified gravity theories, such as Modified Newtonian Dynamics (Milgrom, 1983), predict isotropic lensing at large distances from isolated galaxies where there is no baryonic matter (Milgrom, 2013; Khoury, 2015). A significant detection of anisotropic lensing on large scales would rule out certain modified theories of gravity.

In addition, dark matter halo anisotropy will provide a way to constrain the cross section of self-interacting dark matter. If dark matter interacts with itself, it will lead to scattering interactions that redirect the velocity of each dark matter particle. The resulting velocities are isotropically distributed, despite the anisotropic nature of the initial velocities. A larger self-interacting cross section will cause the halo to be rounder, especially in the inner regions of the halo (Davé et al., 2001; Peter et al., 2013). Similarly, a smaller cross section will result in more elliptical haloes.

In this chapter, we will outline weak lensing and its use as a tool to study dark matter halo anisotropy. Then we will summarise observations that have been made of halo

ellipticity. Finally, we will present an outline of the structure of this thesis.

1.1   Weak Gravitational Lensing

General Relativity predicts the path of a photon will be deflected as it passes by a mass distribution. This effect, known as gravitational lensing, will cause background images to be warped by a foreground mass distribution. Light from a background galaxy, or source, will experience this lensing effect as it passes by a foreground galaxy, or lens, and its dark matter halo. This effect is known as galaxy-galaxy lensing. The manner of distortion experienced by the background galaxy allows us to study the foreground mass distribution. For this reason, gravitational lensing is a powerful tool that can be used to observe matter on a large scale, beyond the extent of light profiles. Lensing is well suited for studying dark matter haloes, which do not emit light and are therefore difficult to observe.

Gravitational lensing can be separated into two regimes: strong lensing and weak lensing. Strong lensing only occurs near massive lenses and causes the source to be split into multiple images. Weak lensing causes the shape of the source to be slightly distorted, and is much more common. Due to its prevalence in the universe, this thesis will utilise weak lensing to study the dark matter haloes of foreground galaxies. This weak lensing effect is imperceptible on a single source and can only be detected as a statistical measurement, which involves stacking thousands to millions of galaxies to obtain a significant detection. Galaxy-galaxy weak lensing is a well-documented phenomenon (Brainerd et al., 1996; Hudson et al., 1998) that promises to increase in precision as large, wide-field imaging surveys become more prominent. This galaxy-galaxy lensing is a proven technique for studying dark matter haloes on galaxy-scales and their isotropic mass profiles (Mandelbaum et al., 2006b; Hudson et al., 2015).

The effect of gravitational lensing on an image can be represented as a matrix transformation. The matrix transforms the source coordinates $(\vec{x})$ to the observed image coordinates $(\vec{x'})$ through the following transformation.

$$\vec{x'} = \frac{1}{(1-\kappa)^2 - \gamma^2} \begin{pmatrix} 1 - \kappa + \gamma_1 & \gamma_2 \\ \gamma_2 & 1 - \kappa - \gamma_1 \end{pmatrix} \vec{x} \tag{1.2}$$

The shear (γ) describes how the image is stretched. It can be broken up into two components that each stretch the source in a certain direction and shrink it in the perpendicular direction. These shear components are related to the total shear through $\gamma^2 = \gamma_1^2 + \gamma_2^2$. The convergence (κ) is how the image is resized isotropically.
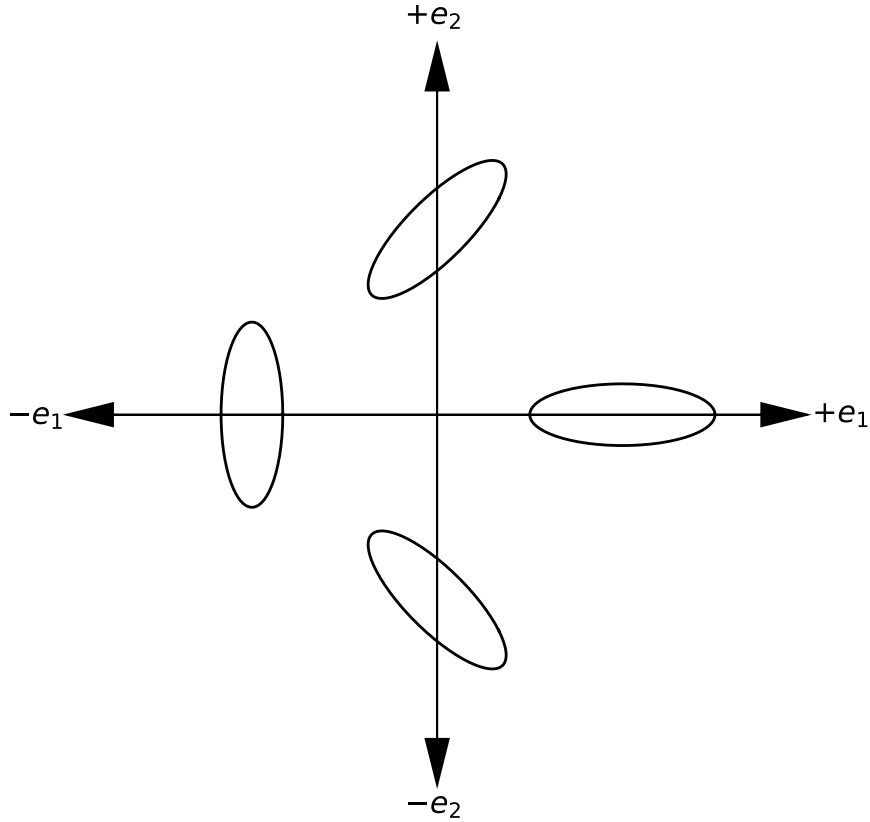
Figure 1.1: The axes of the ellipticity coordinates

The shape is affected by both the shear and convergence, so we cannot measure γ from observations. Instead, we measure the reduced shear, $g = \gamma/(1-\kappa)$ (Bartelmann & Schneider, 2001). In weak lensing, $\kappa \ll 1$ and so we can approximate $g \sim \gamma$. The reduced shear we measure will yield a shape that is represented by two ellipticity coordinates, e_1 and e_2. These coordinates are related to the direction the source is pointing in a similar way to the shear components. The effect each component has on the overall ellipticity of the image can be seen in Figure 1.1. These coordinates are measured in a coordinate system where the x-axis increases along the negative RA axis. The ellipse in each of the directions of the axes depict a shape that is primarily described by one of the ellipticity coordinates. The first coordinate describes the shape in the vertical or horizontal direction. The second coordinate describes the shape in either of the diagonal directions.

We can also compute the tangential shear (γ_t), which describes how the source is stretched either tangentially or radially with respect to the line connecting the source and the lens. This tangential shear is particularly interesting because we can use it to determine the projected excess surface mass density ($\Delta\Sigma(R)$) for spherical mass distributions. First we need to know the critical density (Σ_{crit}). This critical density depends on the angular diameter distance to the lens (D_l), the source (D_s), and between the lens and source (D_{ls}).

$$\Sigma_{crit} = \frac{c^2}{4\pi G}\frac{D_s}{D_l D_{ls}} \tag{1.3}$$

Now we can calculate $\Delta\Sigma(R)$ using

$$\Delta\Sigma(R) = \Sigma_{crit}\gamma_t \tag{1.4}$$

This excess mass density is related to the projected mass density. At a certain radius, R, the excess mass density is the difference between the mean density within a circle of radius R and the density at R.

$$\Delta\Sigma(R) = \overline{\Sigma(< R)} - \overline{\Sigma(R)} \tag{1.5}$$

$$\Delta\Sigma(R) = \frac{1}{\pi R^2}\int_0^R \Sigma(R')2\pi R' dR' - \Sigma(R) \tag{1.6}$$

1.2 Summary of Current Observations

N-body simulations have revealed that dark matter haloes are actually triaxial, and appear elliptical in projection. Simulations by Dubinski & Carlberg (1991) found the distribution of projected ellipticities peaks at $e = 0.5$. However the haloes become rounder when measured ellipticity is measured at larger radii. Warren et al. (1992) study a larger number of haloes in several different simulations. They study the ellipticity distribution in several radial bins and observed the same trend of decreasing ellipticity at larger radii. The peak of the ellipticity distributions tend to $e = 0.25$ beyond 50 kpc. Bailin & Steinmetz (2005) explore the ellipticity of dark matter haloes at lower masses in simulations. They observe a broad range of projected ellipticities with a mean of $e = 0.24$. Simulations have also revealed that more massive haloes tend to be more elliptical (Allgood et al., 2006).

Attempts have been made to observe halo shape using the distribution of satellite galaxies. Satellite galaxies are a useful dynamical tracer of the of the dark matter halo of the central galaxy. The relationship between satellite galaxies and their host haloes has been demonstrated by their usefulness in constraining the dynamical mass (McKay et al.,

2002) and the density distribution (Prada et al., 2003) of their host haloes. Satellite tidal streams have been used to place constraints on the halo shape of the Milky Way (Ibata et al., 2001; Vera-Ciro & Helmi, 2013). Studies have also focused on the distribution of satellite galaxies with respect to the shape of the central galaxy (Brainerd, 2005; Azzaro et al., 2007). A preferential alignment of the satellite distribution along the major axis of the light of the central galaxy is evidence of a non-spherical dark matter distribution. This alignment is strongest for red central galaxies (Yang et al., 2006). Preferential distribution of satellites along the major axis of the dark matter halo has also been confirmed in simulations (Zentner et al., 2005; Libeskind et al., 2007).

Weak lensing has been proposed as another possible method of detecting dark matter halo anisotropy (Natarajan & Refregier, 2000). This method has been used to measure the halo ellipticity of cluster-scale haloes (Evans & Bridle, 2009; Oguri et al., 2010), where the lensing signal is much stronger. Recently, attempts have been made to extend this analysis down to the galaxy-scale. Weak lensing has already been used to constrain the alignment between the galaxy light and the halo (Mandelbaum et al., 2006c; Schrabback et al., 2015).

Normally, the lensing signal from a dark matter halo is considered to be isotropic on average when stacking many galaxies, described by a Navarro-Frenk-White (NFW) profile (Navarro et al., 1997).

$$\rho(r) = \frac{\rho_s}{r/r_s(1 + r/r_s)^2} \tag{1.7}$$

Triaxial haloes in projection will yield an anisotropic weak lensing effect, with a stronger effect along the projected major axis. To account for the anisotropy, we can model the projected mass as a multipole expansion, with a monopole term and a quadrupole term (Natarajan & Refregier, 2000).

$$\Sigma(R, \theta) = \Sigma_0(R) + \Sigma_2(R)\cos(2\theta) \tag{1.8}$$

where θ is defined as the angle measured counter-clockwise from the major axis of the mass distribution. The monopole term is represented by an NFW profile, while the quadrupole term has angular dependence and accounts for the halo ellipticity, e.

$$\Sigma_2(R) = -\frac{e}{2}\eta_0(R)\Sigma_0(R) \tag{1.9}$$

The function $\eta_0(R)$ describes how the quadrupole term is related to the monopole term at different radii. Clampitt & Jain (2016) use

$$\eta_0(R) = \frac{d\log\Sigma_0(R)}{d\log R} = \frac{R}{\Sigma_0(R)}\frac{d\Sigma_0(R)}{dR} \tag{1.10}$$

Similarly, the shear a source experiences can be split into a monopole shear and a quadrupole shear. When studying the monopole shear, as is normally done, we would only be concerned with the tangential shear. However, when studying the quadrupole shear we must take the orientation of the lens into account. Before stacking the lenses, we need to rotate to a coordinate system where the x-axis is aligned with the major axis of the lens. The effect of the quadrupole shear will vary in different locations around the lens, so stacking the lenses without taking their orientation into account would smooth out the quadrupole shear completely. We cannot see the shape of the dark matter halo for each lens. Instead we need to align the coordinate system with something we can observe that is also a reliable proxy for the major axis of the dark matter halo. A reasonable choice is to align the coordinate system along the major axis of the lens light.

This method has been used by several studies in order to obtain a masurement of halo ellipticity. Hoekstra et al. (2004) obtained one of the first detections of dark matter halo ellipticity using weak lensing. They studied 1.2×10^5 lenses and 1.5×10^6 sources selected by magnitude. In their model, the lens light is aligned with the halo, but the ellipticity of the light is related to the ellipticity of the halo through the factor f. They measured a halo ellipticity of $e = 0.33^{+0.07}_{-0.09}$.

Parker et al. (2007) studied halo shape using galaxy-galaxy weak lensing in the Canada-France-Hawaii Telescope Legacy Survey. They select $\sim 2 \times 10^5$ lenses and $\sim 1.3 \times 10^6$ sources based on magnitude. They divided the area surrounding the lens into 4 regions, 2 along the major axis and 2 along the minor axis. By measuring the difference in tangential shear between these regions, they observed an ellipticity of ~ 0.3 at the 2σ level.

More recently, Clampitt & Jain (2016) measured the quadrupole lensing signal around 70,000 luminous red galaxies (LRGs) from the Sloan Digital Sky Survey (SDSS) using shear catalogues from Sheldon et al. (2009). The best fit to their model is a halo ellipticity of $e = 0.24 \pm 0.06$, which rules out no ellipticity at the 4σ confidence level. They performed a similar analysis of 27,000 redMaPPer clusters (Rykoff et al., 2014). The clusters are best fit by an ellipticity of $e = 0.21$ and no ellipticity is ruled out at the 3σ level.

A multipole lensing distribution was used by van Uitert et al. (2017) to study elliptical dark matter haloes. They studied 2,600 group scale haloes with an average halo mass of $M_{200} = 1.50^{+0.25}_{-0.24} \times 10^{13} M_\odot$. They oriented along the major axis of the BCG light and measure the quadrupole shear. Within a range of $40 - 250$ kpc they obtain a best fit halo ellipticity of $e = 0.38 \pm 0.12$. Extending to larger scales, they obtained a halo ellipticity of $e = 0.24 \pm 0.08$ when fitting over a range of $40 - 750$ kpc.

So far, we have discussed previous measurements of dark matter halo ellipticity that were made assuming it was aligning with the lens light. However, we could also make

the assumption that the dark matter halo is aligned with the filaments and surrounding structure. Preferential alignment of the halo with the filament, rather than the galaxy light, has been observed in simulations (Ganeshaiah Veena et al., 2019). Dark matter haloes are assembled hierarchically, with smaller subhaloes merging over time to form larger haloes. Haloes within a filament will accrete subhaloes in a preferential direction along the filament. This causes haloes within a filament to maintain their alignment with the filament, while isolated haloes will experience more radical changes in alignment over time (van Haarlem & van de Weygaert, 1993). This stability could cause filaments to be a more reliable alignment proxy than galaxy light.

1.3   Outline of Thesis

In this work, we use weak lensing to measure the ellipticity of dark matter haloes. In Chapter 2 we discuss the use of galaxy shape measurements from the Canada-France Imaging Survey (CFIS). We will also use both CFIS and SDSS to obtain lens light shapes to use as an alignment proxy. We will also discuss the use of LRG pairs to determine the orientation of filaments. We will study the distribution of source galaxies around the lenses, and infer which methods of alignment are best suited to studying the quadrupole shear.

In Chapter 3 we outline the methods and techniques used to measure halo ellipticity using our weak lensing data. We describe the method used to stack the monopole and quadrupole shear. We develop a model to be used to describe anisotropic dark matter haloes. We then discuss how misalignment between the galaxy light and dark matter halo will affect our model and eventual halo ellipticity measurement. We review two sets of estimators which are used to measure the quadrupole shear, while cancelling any contribution from the monopole. We then present results from an idealised elliptical lens to visualise how these estimators are expected to behave.

In Chapter 4 we discuss the results for both the monopole and quadrupole shear. We discuss values of halo ellipticity derived from fits to the quadrupole estimators and their significance. We evaluate possible sources of systematic effects which may bias our results, including inadequate PSF correction and issues in the shape measurements. Finally, we compare results using CFIS lens light angles to results using lens light angles from SDSS.

We present further discussion of these results in Chapter 5. We revisit information revealed by the distribution of source galaxies in order to account for the effect of satellite galaxies on our results. We discuss results obtained when aligning along filaments and how these compare to results obtained when aligning using the lens light.

We adopt a standard cosmological model with $H_0 = 70$ km s^{-1} Mpc^{-1}, $\Omega_m = 0.3$, and $\Omega_\Lambda = 0.7$.

Chapter 2

Data

The effect of weak lensing on the shape of an individual source galaxy is insignificant compared to the inherent shape of the source. We can only observe the effects of weak lensing by stacking many sources to determine the average overall shear. This effect is still impossible to study for individual lenses, so we also stack a large number of lenses to study the average shear for all lenses in the stack. The shear of these sources and lenses is stacked to cancel any contributions from the random original orientations of the sources. Measurements in weak lensing are dominated by noise, so a large sample of sources and lenses is required in order to obtain significant results. This is even more important when measuring quadrupole shear, which is roughly an order of magnitude less significant than the monopole shear. In this section, we will discuss the source and lens catalogues.

2.1   Sources

A significant measurement of quadrupole shear, and of halo ellipticity, will require a large number of sources. The source catalogue makes use of data from the r-band component of CFIS. CFIS is a wide-field imaging survey designed to compliment existing spectroscopy from SDSS. The r-band component of CFIS will eventually cover 5000 square degrees of high quality imaging data and shape measurements to a depth of 24.1 with a signal-to-noise ratio of 10. CFIS currently covers over 2000 square degrees of the northern hemisphere, containing roughly 46 million sources. This coverage can be divided into 4 contiguous regions, which we call "patches." To save computer time and memory, the weak lensing analysis is performed on each of these individual patches rather than on the entire source catalogue simultaneously. The patches are large enough that any effects from being near

the edge of the source catalogue are minimal. Patch 1 is the largest, containing nearly half of the sources. Patch 4 contains roughly a quarter of the sources, while Patches 2 and 3 contain roughly an eighth.

Shape measurements, necessary for weak lensing, are generated using an early version of ShapePipe (Guinot A., Farrens S., Kilbinger M. et al., in prep), a new shape measurement pipeline being developed by CFIS collaborators at the Centre d'Energie Atomique (CEA) and the Université Paris-Saclay. This technique uses the `ngmix` package (Sheldon, 2015) to perform METACALIBRATION (Huff & Mandelbaum, 2017). After calibration, a model is fit to the image which yields the ellipticity components e_1 and e_2 for each source. Each source will also be assigned a weight which quantifies how well the image is fit by the resulting shape. This weight is useful in weak lensing as it constitutes part of the weighted average when stacking. For each source, the weight is given by

$$w = \frac{1}{2\sigma_{int}^2 + \sigma_{e1}^2 + \sigma_{e2}^2} \tag{2.1}$$

The intrinsic scatter, σ_{int}, represents the shape noise. It has been measured in the data as $\sigma_{int} = 0.34$. The two parameters $\sigma_{e,i}^2$ are the variances of the ellipticity coordinates estimated from the fit.

To convert the shear into a mass distribution, we need the source redshift distribution, $n(z)$. This function describes the probability of a source being found at a given redshift. Determining $n(z)$ for CFIS sources is not straightforward. Currently, CFIS lacks spectroscopy, and photometry is only available in a single band, restricting our ability to calculate photometric redshifts. Instead, we can obtain $n(z)$ using the method described in Lima et al. (2008). We match the CFIS catalogue with the W3 patch of Canada-France-Hawaii Lensing Survey (CFHTLenS), which overlaps with CFIS. CFHTLenS has photometry in the 5 *ugriz* bands. A spectroscopic sample, with *ugriz* photometry, containing objects from CFHTLenS and VIPERS was obtained from H. Hildebrandt (private communication). Galaxies in this sample were reweighted until their distribution in 5-dimensional colour space matched that of the *ugriz* CFIS catalogue. The resulting reweighted $n(z)$ from the sample was then adopted as the $n(z)$ for the CFIS catalogue. This process operates under the assumption that two samples with identical distributions of colours, magnitudes, and other photometric properties, will have the same redshift distribution.

We divide the catalogue into 10 regions and bootstrap sample these regions. We then reweight the bootstrapped catalogue to obtain the uncertainty in $n(z)$. The resulting $n(z)$ is fit by the profile described in equation 2.2. We also create versions of the catalogue that are magnitude limited and fit with the same profile. This is done to account for varying

11

depth across the field. The distribution of parameters as a function of weighted median r-band magnitude is fit by equations 2.3 and 2.4.

We fit the data with a source redshift function of

$$n(z) = \left(A(m) \cdot \frac{z^\alpha \cdot e^{-\left(\frac{z}{z_0(m)}\right)^\alpha}}{\frac{z_0^{\alpha+1}}{\alpha} \cdot \Gamma\left(\frac{\alpha+1}{\alpha}\right)} \right) + \left((1 - A(m)) \cdot \frac{e^{-\frac{(z-\mu)^2}{2\sigma^2}}}{2.5046} \right) \tag{2.2}$$

$$A(m) = -0.4154m^2 + 19.1734m - 220.261 \tag{2.3}$$

$$z_0(m) = 0.1081m - 1.9417 \tag{2.4}$$

where $\alpha = 1.79$, $\sigma = 1.3$, $\mu = 1$ and where m is the median weighted r-band magnitude. This median r-band magnitude is different for each of the 4 patches, so each patch will use a slightly different $n(z)$ and $\Sigma_{crit}^{-1}(z_l)$. The median magnitude for Patch 1 is $m = 22.95$, for Patch 2 it is $m = 22.944$, for Patch 3 it is $m = 22.923$, and for Patch 4 it is $m = 22.952$. The process of reweighting and fitting $n(z)$ was undertaken by I. Spitzer (private communication).

To convert our observed shear to a mass density, we need to know the critical density. We use the redshift of the lens and the redshift of the source in order to calculate the angular diameter distance to each. We can then use Equation 1.3 to calculate Σ_{crit}. Unfortunately, in CFIS we do not have redshifts for the sources. Instead, we will calculate a function for the critical density that depends only on the redshift of the lenses, which we will discuss in the next section. We utilise the method described by Viola et al. (2015). Using the redshift distribution, $n(z)$, for our source sample in CFIS, we can calculate the inverse of the critical density. This involves using the probability distribution and the angular diameter distances to integrate from the lens redshift to infinity.

$$\langle \Sigma_{crit}^{-1}(z_l) \rangle = \int_{z_l}^{\infty} \frac{D_l(z_l)D_{ls}(z_l, z_s)}{D_s(z_s)} n(z_s) dz_s \tag{2.5}$$

This can be calculated for each lens, inverted, and incorporated into the weighted average to obtain the excess mass density, $\Delta\Sigma$. The source redshift distribution in CFIS and the critical density function are shown in Figure 2.1.

2.2 Lenses

For our lens sample, we select LRGs from the Baryon Oscillation Spectroscopic Survey (BOSS) (Dawson et al., 2013) component of SDSS-III (Eisenstein et al., 2011). These
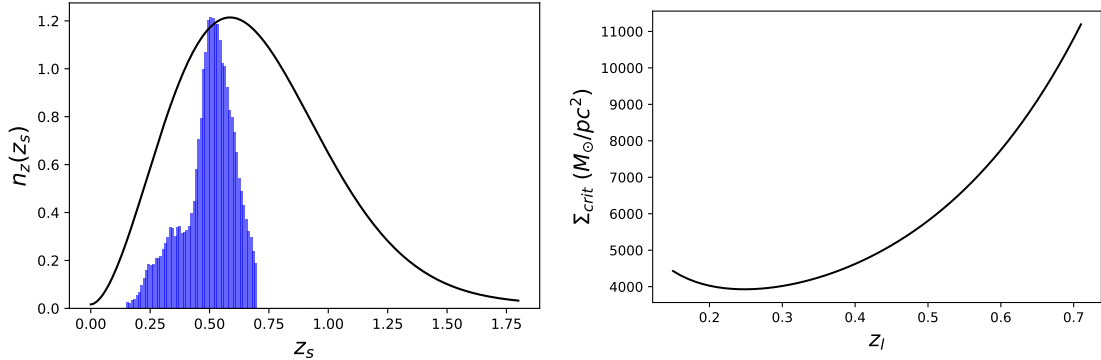
Figure 2.1: Source redshift distribution and critical density function used in this paper. The solid black line in the left subplot represents the source redshift distribution described in Equation 2.2. The histogram in blue represents the redshift distribution of the lenses. On the right is the corresponding critical density function.

LRGs are selected within several magnitude and colour criteria, and span a redshift range of $0.15 < z < 0.7$. Only LRGs that overlap with the current CFIS footprint were used. This resulted in a lens sample of approximately 146,000 lenses.

We use LRGs as lenses because they reside in massive dark matter haloes, with a typical halo mass on the order of $10^{13} - 10^{14} h^{-1} M_\odot$ (Zheng et al., 2009). The contribution from quadrupole shear, which we need to measure in order to detect halo ellipticity, is quite small compared to the monopole shear. A more massive halo will contribute a stronger lensing signal, which should make it easier to detect significant quadrupole shear. More massive haloes also tend to be more elliptical (Allgood et al., 2006), which could lead to a more significant measurement of halo ellipticity. Finally, LRGs provide a reliable method of aligning our lensing measurements. The distribution of satellite galaxies, which may trace the dark matter halo, are more aligned with the galaxy light for red central galaxies (Yang et al., 2006). We expect the light of the LRGs to be well aligned with their dark matter haloes, making the major axis of the light a reliable proxy for the major axis of the dark matter halo.

There are several ways to measure the orientation of the lenses to properly align them before stacking. One way is to make the assumption that the light from the LRG is aligned with the major axis of the dark matter. Both CFIS and SDSS have shape measurements which provides two options of lens position angles, the angle from the x-axis of the image to the major axis of the light. We could also assume the dark matter haloes are more likely to be aligned with the large scale structure rather than the galaxy light. We could group
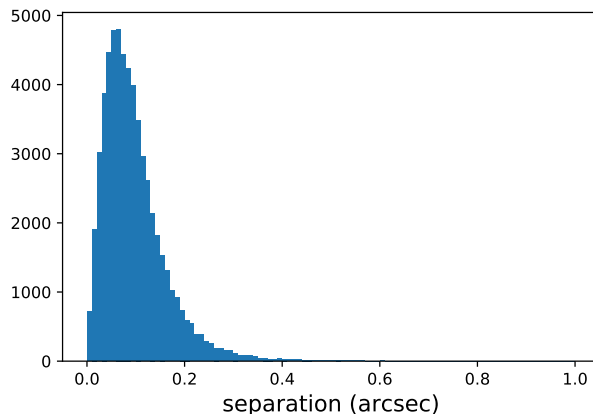
13

Figure 2.2: Histogram of the separation of the positions of the LRGs in BOSS and CFIS.

the LRGs into pairs and take the position angle to the pair counterpart as an approximate measure for a filament. This leaves us with three ways to align the lenses: light angle from CFIS, light angle from SDSS, and LRG pair angle. Each of these alignment proxies will be discussed in the subsequent sections.

2.2.1 CFIS Lens Position Angles

Information about the shape and orientation of each object in CFIS was obtained using SExtractor (Bertin & Arnouts, 1996). To obtain lens position angles for the LRGs, we match on the LRG catalogue with CFIS on RA and DEC. For each LRG, the separation is calculated for all objects in CFIS within 1 arcsecond of the position of the LRG in BOSS. The closest object is then chosen and the lens position angle from that object in CFIS is used for the LRG. A histogram of the separation of the positions of the LRGs in BOSS and CFIS is displayed in Figure 2.2. The median separation of the matched positions is 0.08 arcseconds and the vast majority are within 0.5 arcseconds.

Now that we have matched these LRGs with objects in CFIS, we need to decide which angle to use as the lens position angle. There are a few different angles listed for each object in CFIS. The four types of angles listed in CFIS and their descriptions in the header are: THETA (angle counter-clockwise from image x-axis), THETA WORLD (angle counter-clockwise from world x-axis), THETA SKY (position angle East of North, native), and THETA J2000 (position angle East of North, J2000).

An image of a galaxy from CFIS is shown in Figure 2.3. This galaxy was chosen because
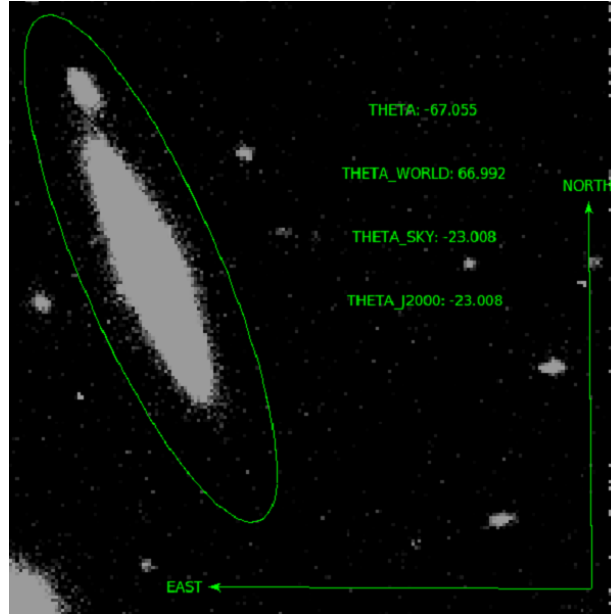
14

Figure 2.3: A galaxy from CFIS. This galaxy was chosen because it was very elliptical, which would make the major axis easier to identify. The coordinate system is represented by arrows pointing North and East. The 4 angles from SExtractor are printed as text on the image.

it was very elliptical, which would make the major axis easier to identify. The coordinate system is represented on the image by arrows pointing North and East. The 4 angles from SExtractor are printed as text on the image. The angles THETA SKY and THETA J2000 are given as -23°. This angle is supposed to be East of North, but the angle of -23° would be accurate if this was West of North. After comparing several other lenses, it seems that these angles are actually West of North. However, the angle THETA appears to be accurate. This angle is given as -67° counter-clockwise from the x-axis, or 67° clockwise from the x-axis. For the remainder of the project, we will use the angle THETA.

In order to resolve the confusion between the angles, we can compare the position angles from SExtractor to position angles derived from the ShapePipe ellipticities. This is done using $\theta = \frac{1}{2}\arctan(e_2/e_1)$. These angles are both measured counter-clockwise from the x-axis. Not all lenses in our sample have well defined e_1 and e_2. Some lenses are too large or too bright, which leads to issues with the shape fit from ShapePipe. Only about 1/3 of the lenses, or about 58,000, have well defined e_1 and e_2 and have a match on the CFIS SExtractor catalogues within 1 arcsecond.
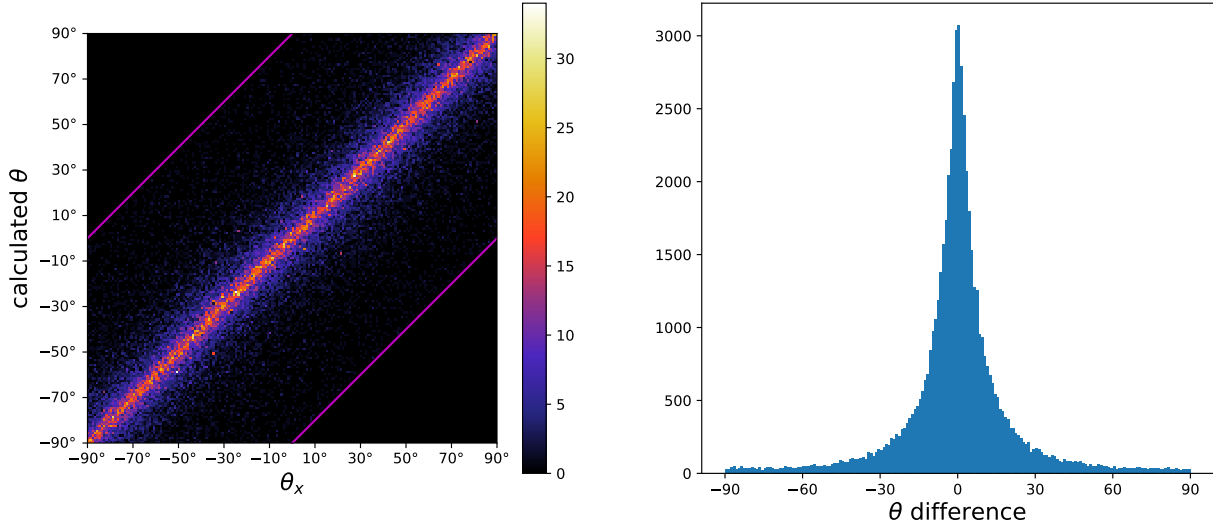
15

Figure 2.4: Comparison of lens angles from CFIS. Only the 58,000 lenses with a match within 1 arcsecond are included. The lens angle from SExtractor, θ_x, is compared with the angle calculated using $\theta = \frac{1}{2}\arctan(e_2/e_1)$. On the left is a scatter plot with points combined into $1° \times 1°$ bins. On the left is a histogram of the differences between these angles.

We compare these angles in Figure 2.4. Only the 58,000 lenses with a match within 1 arcsecond are included. The subplot on the left is a scatter plot of calculated angle vs measured angle. These points were combined into $1° \times 1°$ bins. In addition to this, points near the corners $(-90°, 90°)$ and $(90°, -90°)$ were corrected. Small differences in angle can lead to large differences on the scatter plot. For example, a lens may have a SExtractor angle of $89°$, but a ShapePipe angle of $-88°$. Due to the symmetry of the lenses, lens position angles separated by $180°$ are equivalent. So an angle of $-88°$ can also be written as $92°$, and this difference of $177°$ is actually only a difference of $3°$. This correction is displayed as purple boundary lines on the scatter plot. In addition to the scatter plot, the subplot on the right is a histogram of the differences between these angles. The same correction was applied to the data in the histogram. For most lenses, the difference between the SExtractor and ShapePipe light position angles is close to 0. The semi-interquartile range of the difference is $13.8°$ and the standard deviation is $21.6°$.
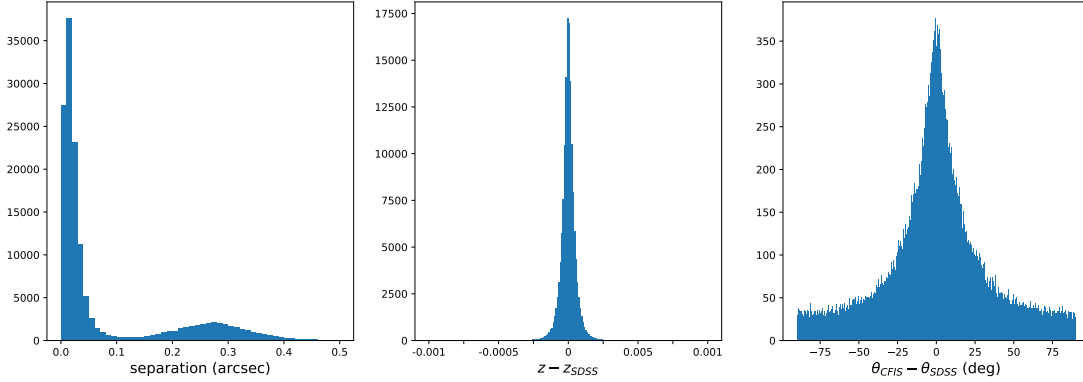
16

Figure 2.5: A comparison of LRGs in CFIS and SDSS. Left: separation in arcseconds. Centre: difference in redshift. Right: difference in position angle from the x-axis.

2.2.2 SDSS Lens Position Angles

When using lens position angles from CFIS, the shape measurements of the sources and lenses are both derived from the same imaging. It is possible that issues with the shape measurements, for example inadequate PSF correction, could lead to a correlation between the lens and source shapes. This correlation could lead to an observed alignment that could affect our weak lensing results. To provide an alternate test, and an independent source of lens position angles, we can perform the quadrupole shear measurement using position angles from SDSS. First, all LRGs were selected from the DR16 release of SDSS using `z_nosqo>0` and `sourceType=LRG`. The resulting list of LRGs were then matched on RA and DEC to our list of LRGs that overlap with CFIS. These LRGs were fit with both an exponential and a de Vaucouleurs profile. From the fit with the highest likelihood, the angle was added to the corresponding entry in the LRG sample. The angles from SDSS are defined East of North. In order to compare them to the CFIS angles which are defined as counterclockwise from the x-axis, $\pi/2$ was added to the SDSS angles. It is worth noting that SDSS imaging is shallower than CFIS, so we might expect their position angles to less accurate than the angles from CFIS.

A comparison of the LRGs in CFIS and SDSS is displayed in Figure 2.5. In addition to the position angle from the x-axis, the RA, DEC, and redshift were also obtained from BOSS. The BOSS LRGs are from an earlier data release of SDSS. This has led to differences in the positions and redshifts. In the left subplot, the separation between the coordinates from CFIS and the coordinates from BOSS is plotted. In the centre subplot, the difference in redshift from both surveys is also included. Most LRGs have a separation between both

17

surveys of less than 0.1 arcseconds and a difference in redshift of less than 0.005. This suggests that the LRGs are well matched between the catalogs. Finally, the right subplot displays the difference in position angle from the x-axis in both surveys. Most angles are similar, however, there is a significant number of LRGs that have a substantially different angle in SDSS than in CFIS. The semi-interquartile range of the difference is 31.4° and the standard deviation is 33.6°.

2.2.3 LRG Pair Angles

Later in this thesis, we will discuss results relating to pairs of LRGs and the lensing signal that is obtained when aligning along the axis connecting these pairs. Aligning along the axis connecting the LRGs offers an alternative measure of the quadrupole as opposed to aligning along the major axis of the light. We group the LRGs into pairs in order to use them as a proxy for the filaments. Grouping LRGs into pairs has been demonstrated as a reliable method to detect filaments (Epps & Hudson, 2017; Yang et al., 2020). We explore these LRG pairs in Chapter 5.2. In this section, we will first explain how to calculate the LRG pair angle and how this angle compares to the previously discussed lens position angle.

Filaments can be straight, and therefore lie along the axis connecting the LRG pair, or they can be warped. Identifying LRG pairs is not a reliable method of approximating the filament if it is warped, as warped filaments will not lie along the LRG pair axis. Whether a filament is more likely to be straight or warped depends on the separation between the LRGs. Simulations by Colberg et al. (2005) identify 5-15 Mpc/h as the range in which most filaments are expected to be straight. Warped filaments cover a broader range distribution, but extend to much further pair separations, where straight filaments are unlikely. Clampitt et al. (2016) divide their sample of LRG pairs into two radial ranges. They detect stronger shear signal from filaments within the 6-10 Mpc/h sample than for the 10-14 Mpc/h sample. Moreover, Yang et al. (2020) and Epps & Hudson (2017) have also studied the properties of filaments in the range 6-10 Mpc/h. Therefore, we adopt a projected separation range of 6-10 Mpc/h for our LRG pair sample.

For each LRG, we limit the set of possible LRG pair members to $\Delta z = 0.002$ and a projected separation range of $6 - 10$ Mpc/h. We identify the pair counterpart as the closest LRG within this region. Only 100,000 LRGs have a pair counterpart using this definition. The angle between the line connecting the LRG pair members and the x-axis, measured counterclockwise from the x-axis, will be referred to as θ_{pair}.

Figure 2.6 displays a comparison of θ_{pair} and θ_x, the position angle of the LRG light from
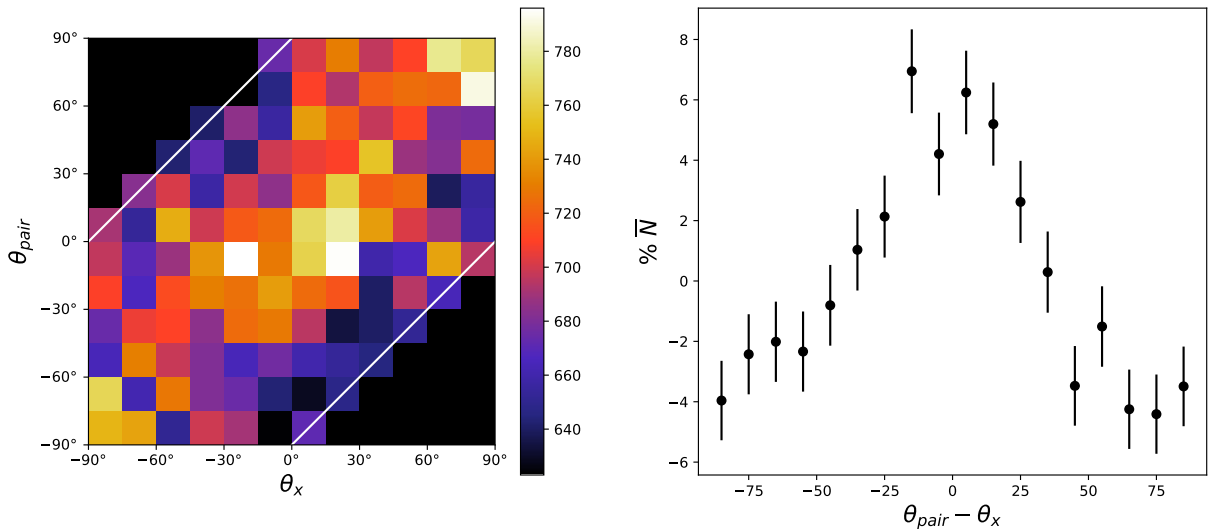
Figure 2.6: Comparison of θ_{pair}, the angle between the x-axis and the LRG pair counterpart, and θ_x the position angle of the LRG's light. Left: the points from a scatter plot binned in 2D. Right: normalised histogram of differences between the angles in 10 degree bins.

the CFIS SExtractor catalogue. In order to make any correlation more visibly apparent than a scatter plot, the points in a scatter plot of θ_{pair} and θ_x were binned in 2D. This 2D binning is visible in the left subplot. A correction was applied to account for points at $(-90°, 90°)$ and $(90°, -90°)$. The boundary of this correction is visible as white lines. On the right, the differences between the angles are binned into 10 degree bins. Fitting $\cos(2\theta)$ to the histogram will allow us to quantify how significantly the angles are related. This fit yields an amplitude of $4.7 \pm 0.5\%$. This suggests a correlation between the orientation of the light and the orientation of the filament. However, it is quite weak.

2.3 Azimuthal Distribution of Sources

Later in this thesis, we will discuss how the results could be affected by the possible inclusion of satellite galaxies in our source sample. Due to the lack of redshifts associated with the sources, there is no way to determine if a given source is actually behind the lens. Thus it is possible that some of the sources around the lens are actually satellite galaxies. If this is the case, we expect there to be an excess of sources along the lens major axis and a deficit along the lens minor axis. In this section, we will discuss the azimuthal distribution
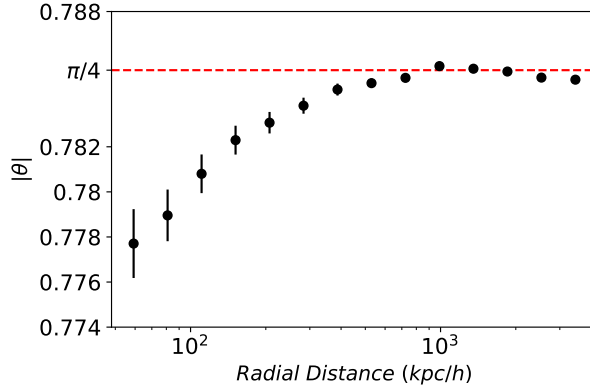
Figure 2.7: Average source position angle from lens light major axis over different radial ranges.

of sources around the lenses, and quantify what fraction of our source sample are actually satellite galaxies.

For each lens, the differences between the positions of the sources and the position angle of the lens light were calculated. The sources were binned radially and a mean average of the source position angle with respect to the lens major axis was calculated. Sources were binned starting at 50 kpc, as source counts become inaccurate near the lens due to contamination from the lens light. Figure 2.7 displays the results of this average as a function of distance from the centre of the lens. The angle displayed is the angle from the major axis, which can vary from 0 to $\pi/2$. If sources were uniformly distributed, this angle should average to $\pi/4$. Far away from the lens, the source position angle averages to $\pi/4$. Closer to the lens the average decreases as more sources are found closer to the major axis. Based on these results, we can conclude that our lenses are aligned correctly.

Using the angle of the light from the CFIS SExtractor catalogue, the lenses were rotated to a coordinate system where the major axis of the light is aligned with the x-axis. The sources were counted in 16 angular bins around the lenses for all LRGs. Only sources within 50-250 kpc were counted. These source counts were weighted by the shape measurement weight. For each angular bin, the uncertainty is the square root of the number of sources in the bin. Results are displayed in the left subplot Figure 2.8. The source distribution exhibits a quadrupole dependence, with more sources along the major axis and less along the minor axis. Fitting a function of the form $\cos(2\theta)$ will allow us to quantify this quadrupole. The amplitude of the source galaxy azimuthal distribution function from the fit is 1.5 $\pm$ 0.3%.
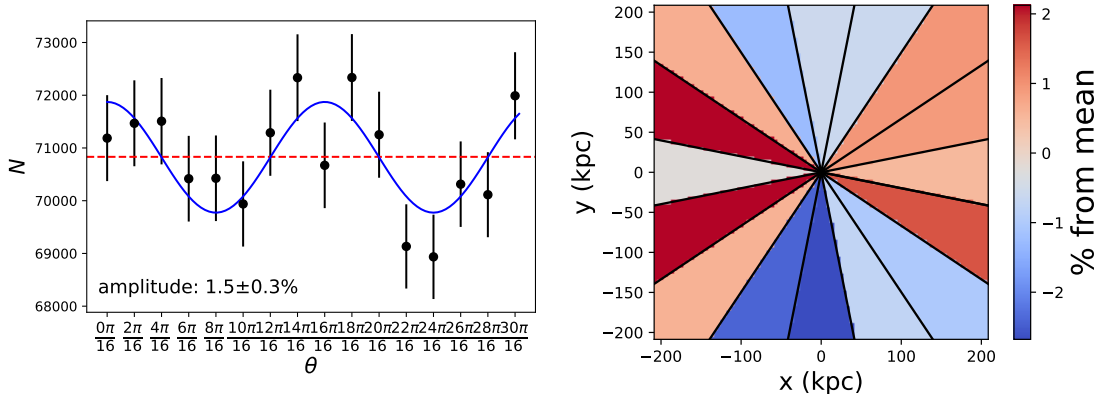
Figure 2.8: Source counts in 16 angular bins around the lenses within 50-250 kpc using CFIS position angle. The counts as a function of angle from the LRG major-axis are displayed on the left. A function of the form $\cos(2\theta)$ was fit with the amplitude as a free parameter. The subplot on the right displays the angular bins with colour according to their deviation from the mean.

To make these results easier to visualise, we can plot these results in 2D. For each angular bin around the lens the percentage difference from the mean is calculated and plotted. We expect bins along the x-axis to be above the mean and bins along the y-axis to be below the mean. The right subplot of Figure 2.8 displays the count in each angular bin, with colour according to deviation from the mean.

We can also repeat the process used to generate Figure 2.8, but using the position angle from SDSS instead of from CFIS. Results using the SDSS lens angle are displayed in Figure 2.9. The quadrupole dependence has an amplitude of $1.1 \pm 0.4\%$. The lower amplitude of azimuthal variation suggests that the CFIS position angles are more accurate than the SDSS ones, as one might expect due to the deeper CFIS imaging.

We can also repeat the process used to generate Figure 2.8, but using the LRG pair position angle instead of the CFIS major axis position angle of the light. Results are displayed in Figure 2.10. Due to the larger extent of the filaments, sources from 50-600 kpc were included in the counts. While we saw significant agreement between the source distribution and the $\cos(2\theta)$ fit in Figure 2.8 for the CFIS angles, here the results are consistent with zero. For the LRG pairs, the fit amplitude is $0.3 \pm 0.2\%$. It is possible that the satellite galaxies are more aligned with the lens galaxy light than with the filament. This could also be due to the inclusion of sources far from the lens, where finding satellites becomes increasingly unlikely.
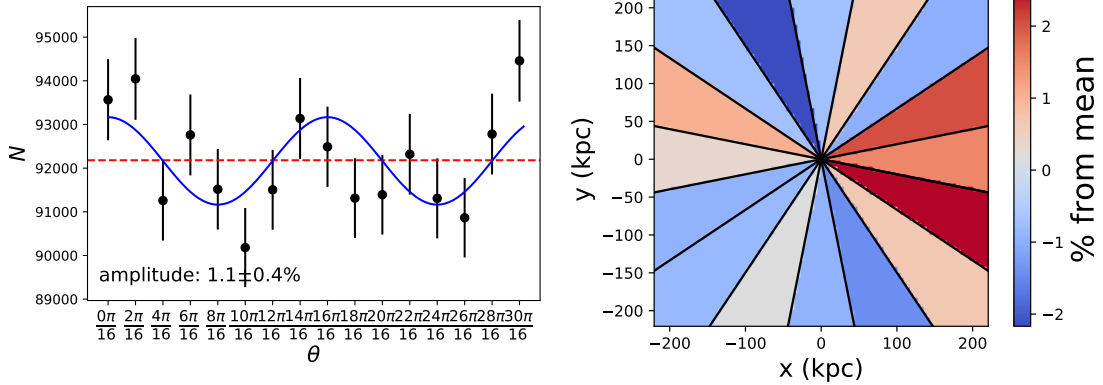
21

Figure 2.9: Source distribution when aligning by SDSS position angle. The counts include sources within 50-250 kpc from the lens.
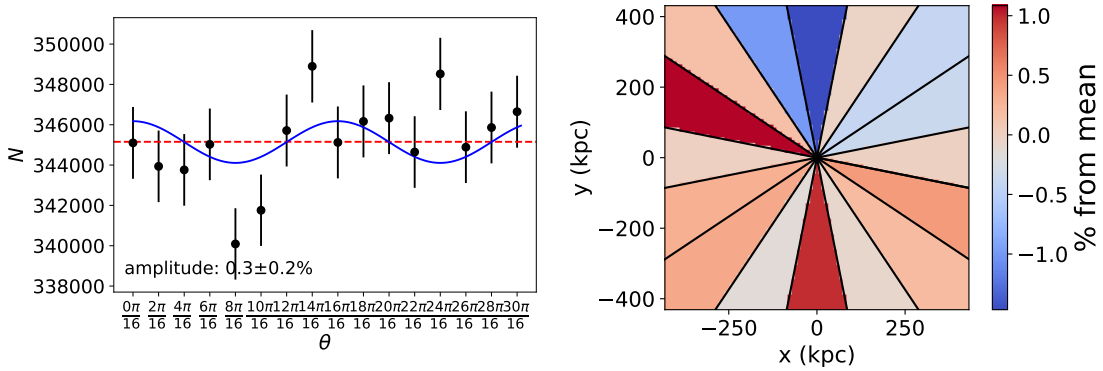

Figure 2.10: Source distribution when aligning by LRG pair angle. The counts include sources within 50-600 kpc from the lens.
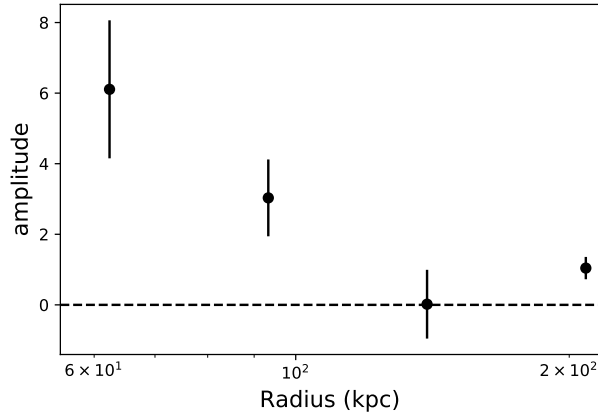
Figure 2.11: Amplitude fit to azimuthal source distribution as a function of radius. A line of 0 amplitude is represented by a dashed line.

Rather than counting all sources within the range, this process of amplitude fitting can be repeated in distinct radial bins. Sources are preferentially distributed in bins along the major axis. This preferential alignment is more prominent for radial bins closer to the lens. To quantify this radial dependence, we fit $\cos(2\theta)$ for all angular bins at a certain radius. Results are visible in Figure 2.11. The amplitude of the $\cos(2\theta)$ dependence varies with the radius. This dependence is quite significant at a distance of 60 kpc from the lens, but descreases as distance from the center increases.

We observe a preferential distribution of sources along the major axis of the light. Using the CFIS SExtractor angle we observe an amplitude of $1.5 \pm 0.3\%$ in the $\cos(2\theta)$ dependence of the source distribution. If satellites trace the halo, this suggests that the dark matter halo is well aligned with the lens light. Therefore, we will primarily align along the lens light when stacking to measure the quadrupole shear. In addition to their usefulness as a possible proxy for shape of the dark matter haloes, satellite galaxies are also a potential source of contamination for our shear measurements. Satellite galaxy orientations are expected to be preferentially aligned with the central galaxy (Schneider & Bridle, 2010; Georgiou et al., 2019), which could lead to a radial bias in the shear. The role of satellites as a potential systematic effect will be discussed further in Section 5.1.

23

Chapter 3

Methods

In this chapter, we will explain how to use our catalogues of lenses and sources to calculate the halo ellipticity. First, we will describe the monopole and quadrupole shear. We use the monopole shear to obtain a mass density profile, $\Delta\Sigma(R)$. We then fit a model to this profile. This model will describe the mass of the halo and its concentration. We then extend the model to describe halo ellipticity. We will also discuss the effects of misalignment between the dark matter halo and the galaxy light, and how this is accounted for in the model. Then we will discuss two sets of quadrupole estimators. These estimators enable us to visualise the quadrupole shear in radial bins, and are designed to maximise the quadrupole signal while minimising any contribution from the monopole shear. Finally, we will examine how these estimators behave in an ideal elliptical system.

3.1 Calculating Shear

Before we can measure the halo ellipticity, we first need to determine the mass and concentration of the halo. This is done by measuring the monopole shear, which is related to the shear in the direction perpendicular to the line connecting the lens and the source. In order for the ellipticity coordinates to be useful we need to determine the angle between the x-axis and the line connecting the lens and the source (α). We can determine the angle on the sky of each source around a given lens, provided we have RA and DEC. We can rotate the ellipticity coordinates and convert them to tangential shear (γ_t) and cross shear ($\gamma_\times$).

$$\begin{pmatrix} \gamma_t \\ \gamma_\times \end{pmatrix} = - \begin{pmatrix} \cos(-2\alpha) & -\sin(-2\alpha) \\ \sin(-2\alpha) & \cos(-2\alpha) \end{pmatrix} \begin{pmatrix} \gamma_1 \\ \gamma_2 \end{pmatrix} \tag{3.1}$$

We assume that galaxy ellipticity is isotropically distributed in the absence of gravitational shear. Any net tangential shear around the centre of the lensing galaxy is considered gravitational shear which is related to the projected surface mass density. This is commonly calculated as a weighted average of the source galaxy ellipticities. All sources have a weight value, w, that describes the quality of the source's shape measurement. In order to down-weight lens-source pairs which are close in redshift, we also weight each lens-source pair by $W = (\langle \Sigma_{crit}(z_l) \rangle^{-1})^2$ (Sheldon et al., 2004). The excess mass density is given by

$$\langle \Delta \Sigma(R) \rangle = \frac{\sum w_j \gamma_{t,j} \Sigma_{crit,i,j} W_{i,j}}{\sum w_j W_{ij}} \tag{3.2}$$

where the sum is over all lenses, i, and sources, j, in a given radial bin. Shape measurements of these sources will have some shape noise that will eventually translate into uncertainty in the excess surface mass density profile. Each source will have an uncertainty σ_e that depends on the weight w assigned to the source by the shape fitting algorithm.

$$\sigma_e^2 = \frac{\sigma_{int}^2}{(w/w_{max})} \tag{3.3}$$

The intrinsic uncertainty in the shape is $\sigma_{int} = 0.34$ and the maximum weight is $w_{max} = 4$. The uncertainty in the shape of each source galaxy will contribute to the uncertainty in the resulting mass density from the monopole.

$$\sigma(R) = \frac{\sqrt{\sum (\Sigma_{crit} W_{crit} \sigma_e w)^2}}{\sum W_{crit} w} \tag{3.4}$$

Now that we have described how to measure the monopole shear, we will next describe how to measure the quadrupole shear. We have broken up the process of stacking the quadrupole shear into 3 steps. These are

1. Convert RA and DEC to Cartesian x and y

2. Rotate the coordinate system so the new x-axis is aligned with the lens light major axis

3. Perform the quadrupole shear measurement

The first step involves converting from RA and DEC to a Cartesian coordinate system. The lens is set at (0,0). The distance from the lens to all sources is calculated depending on the lens coordinates (RA_1, DEC_1) and the source coordinates (RA_2, DEC_2).

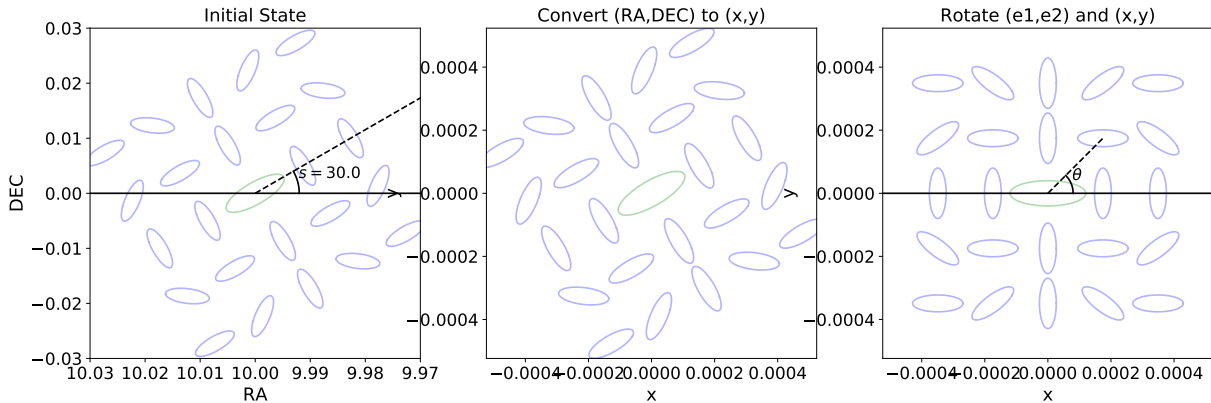$$x = -(RA_2 - RA_1) \cos(DEC_1) \tag{3.5}$$

Figure 3.1: A diagram of the three step process for a single lens. The green ellipse at the centre represents the lens while the blue ellipses represent the sources. The leftmost subplot displays the system in its initial state as it appears on the sky. The central subplot displays the system after converting to a Cartesian coordinate system. The rightmost subplot displays the system after rotating the coordinate system.

$$y = \mathrm{DEC}_2 - \mathrm{DEC}_1 \tag{3.6}$$

RA increases until reaching $360°$ at which point it becomes $0°$. It is possible there may be a lens-source pair that spans this 360-0 transition. We need to add a correction to account for this possibility.

$$\mathrm{RA}_2 = \begin{cases} \mathrm{RA}_2 + 2\pi & \mathrm{RA}_1 - \mathrm{RA}_2 > \pi \\ \mathrm{RA}_2 & |\mathrm{RA}_2 - \mathrm{RA}_1| < \pi \\ \mathrm{RA}_2 - 2\pi & \mathrm{RA}_2 - \mathrm{RA}_1 > \pi \end{cases} \tag{3.7}$$

For the second step, we need to rotate the coordinate system to align the lens light major axis with the x-axis. For every source, we can calculate its position angle α by taking $\arctan(y/x)$. For each source, we need to rotate (x, y) and (e_1, e_2).

$$\begin{pmatrix} x' \\ y' \end{pmatrix} = \begin{pmatrix} \cos(-\alpha) & -\sin(-\alpha) \\ \sin(-\alpha) & \cos(-\alpha) \end{pmatrix} \begin{pmatrix} x \\ y \end{pmatrix} \tag{3.8}$$

$$\begin{pmatrix} e_1' \\ e_2' \end{pmatrix} = \begin{pmatrix} \cos(-2\alpha) & -\sin(-2\alpha) \\ \sin(-2\alpha) & \cos(-2\alpha) \end{pmatrix} \begin{pmatrix} e_1 \\ e_2 \end{pmatrix} \tag{3.9}$$

Once these two steps have been performed, we can calculate the quadrupole for this lens using our estimators, which are described further in Sections 3.4 and 3.5. A diagram of
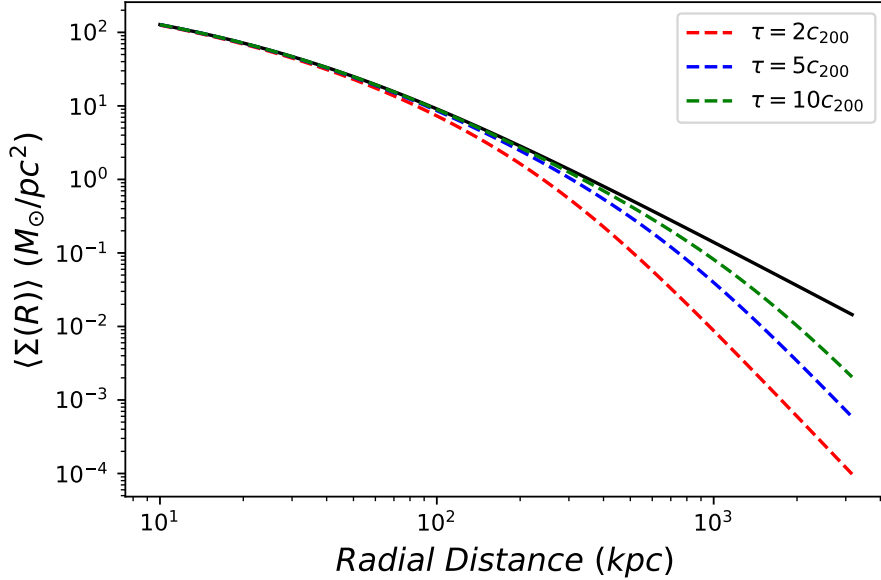
26

Figure 3.2: Truncated $\Delta\Sigma_{NFW}(R)$ profile for several different values of τ.

the three step process for a single lens is displayed in Figure 3.1. This particular system has a lens position angle of $s = 30$, but this process works for all lens position angles. In the state depicted in the right subplot, the quadrupole shear can be calculated for this lens and incorporated into the weighted average.

3.2   Model

The model consists of a 1-halo term $(\Delta\Sigma_{1h})$ which describes the matter associated with the lens galaxy. Normally, we would also include an offset group term to account for lenses that reside within subhaloes inside a larger host halo. However, few of the LRGs will be satellite galaxies. A 2-halo herm is often included as well. This accounts for lensing signal from neighboring haloes, which is normally a significant effect quite far from the center of the halo. This term will not be significant within the radial range we are concerned with.

The 1-halo term is comprised of the contribution from the stellar mass of the galaxy and the mass of the galaxy's dark matter halo. The stellar mass is treated as a point mass term.

$$\Delta\Sigma_*(R) = M_*/\pi R^2 \qquad (3.10)$$

27

We also require a term to describe the dark matter halo in the 1-halo term. Normally, an NFW profile is used to describe the density profile of a dark matter halo. However, the mass of the NFW profile does not converge when integrated to an infinite radius. Instead, we use a truncated NFW profile from Baltz et al. (2009) to describe the dark matter halo, which has a well defined total mass. The truncated NFW profile is

$$\rho(x) = \frac{M_0}{4\pi r_s^3} \frac{1}{x(1+x)^2} \frac{\tau^2}{\tau^2 + x^2} \tag{3.11}$$

where $x = r/r_s$ and $M_0 = 4\pi\rho_s r_s^3$. The truncation factor, $\tau = r_t/r_s$, describes the radius where the truncation term begins to dominate. The scale radius of the halo, r_s, is related to the virial radius (R_{200}) through the concentration (c_{200}). The virial radius is the radius in which the average density is 200 times the critical density of the universe (ρ_c). This is related to the virial mass M_{200}.

$$M_{200} = \frac{4\pi}{3} R_{200}(200\rho_c) \tag{3.12}$$

So if we know c_{200} and M_{200} we can calculate the scale radius.

$$r_s = R_{200}/c_{200} = \left(\frac{3}{4\pi} \frac{1}{200\rho_c} M_{200} \right)^{1/3} /c_{200} \tag{3.13}$$

The scale density, p_s, is related to the critical density and also depends on the concentration.

$$p_s = \frac{200}{3} \frac{c_{200}^3}{\ln(1 + c_{200}) - \frac{c_{200}}{1+c_{200}}} \rho_c \tag{3.14}$$

We parametrise the NFW profile using only M_{200} and c_{200}. For an NFW profile with a given M_{200} and c_{200}, we can find r_s using Equation 3.13 and ρ_s using Equation 3.14.

The projected surface mass density of the truncated NFW profile from Baltz et al. (2009) at a distance R from the centre is

$$\Sigma(x) = \frac{M_0}{r_s^2} \frac{\tau^2}{2\pi(\tau^2 + 1)^2} \left\{ \frac{\tau^2 + 1}{x^2 - 1}[1 - F(x)] + 2F(x) - \frac{\pi}{\sqrt{\tau^2 + x^2}} + \frac{\tau^2 - 1}{\tau\sqrt{\tau^2 + x^2}} L(x) \right\} \tag{3.15}$$

Two special functions are defined

$$F(x) = \begin{cases} \frac{-\ln(1/x - \sqrt{1/x^2 - 1})}{\sqrt{1 - x^2}} & \text{if } x < 1 \\ 1 & \text{if } x = 1 \\ \frac{\cos^{-1}(1/x)}{\sqrt{x^2 - 1}} & \text{if } x > 1 \end{cases} \tag{3.16}$$

and

$$L(x) = \ln\left(\frac{x}{\sqrt{\tau^2 + x^2} + \tau}\right) \tag{3.17}$$

Equation 3.15 gives the mass density, but we are actually interested in the excess mass density. This can be obtained from the mass density.

$$\Delta\Sigma_{NFW}(r) = \frac{1}{\pi r^2}\int_0^r 2\pi r'\Sigma_{NFW}(r')dr' - \Sigma_{NFW}(r) \tag{3.18}$$

$$\Delta\Sigma_{NFW}(r) = \frac{M_{proj}(r)}{\pi r^2} - \Sigma_{NFW}(r) \tag{3.19}$$

The projected mass within a radius r is

$$M_{proj}(x) = M_0\frac{\tau^2}{(\tau^2 + 1)^2}\left\{[\tau^2 + 1 + 2(x^2 - 1)]F(x) + \tau\pi +\right.$$
$$\left.(\tau^2 - 1)\ln\tau + \sqrt{\tau^2 + x^2}\left[-\pi + \frac{\tau^2 - 1}{\tau}L(x)\right]\right\} \tag{3.20}$$

Truncated $\Delta\Sigma_{NFW}(R)$ profiles are plotted in Figure 3.2 for several different values of τ. The total one-halo term is due to the stellar mass term from Equation 3.10 and the dark matter term from Equation 3.19.

$$\Delta\Sigma_{1h} = \Delta\Sigma_* + \Delta\Sigma_{NFW} \tag{3.21}$$

Now we can extend this model to account for the halo ellipticity. The mass density of the anisotropic halo can be split into a monopole, described by the truncated NFW profile, and a quadrupole term. This density function is described in Equation 1.8 and can also be written

$$\Sigma(R, \theta) = \Sigma_0(R)\left[1 - \frac{e}{2}\eta_0(R)\cos(2\theta)\right] \tag{3.22}$$

In order to calculate the quadrupole, we need the derivative of the monopole, $\Sigma_0'(R)$. Baltz et al. (2009) gives this as

$$\Sigma_0'(x) = \frac{M_0}{r_s^2}\frac{\tau^2}{2\pi(\tau^2 + 1)^2}\left\{\frac{-2x(\tau^2 + 1)}{(x^2 - 1)^2} + \frac{\tau^2 + 1}{x^1 - 1}\left[\frac{2x}{x^2 - 1}F(x) - F'(x)\right] - 2F'(x)\right.$$
$$\left.+ \frac{\pi x}{(\tau^2 + x^2)^{3/2}} + \frac{\tau^2 - 1}{\tau\sqrt{\tau^2 + x^2}}\left[L'(x) - \frac{x}{\tau^2 + x^2}L(x)\right]\right\} \tag{3.23}$$

$$F'(x) = \begin{cases} \frac{1}{x(x^2+1)^2}\left[x^2 - x^3\sqrt{\frac{1}{x^2}-1}\ln\left(\frac{1}{x}-\sqrt{\frac{1}{x^2}-1}\right)-1\right] & \text{if } x < 1 \\ 0 & \text{if } x = 1 \\ \frac{\sqrt{x^2-1}-x^2\cos^{-1}(1/x)}{x(x^2-1)^{3/2}} & \text{if } x > 1 \end{cases} \tag{3.24}$$

$$L'(x) = \frac{\tau}{x\sqrt{\tau^2 + x^2}} \tag{3.25}$$

3.3 Misalignment Probability

Earlier, we discussed observed preferential alignment between central galaxies and their host haloes. In practice, however, there is often some degree of misalignment between the light from the galaxy and its host halo. When stacking, the galaxy light is assumed to be aligned with the dark matter halo. However, it is possible that the angle between the light and the dark matter halo, which we will call θ_{mis}, is non-zero.

Simulations by Okumura et al. (2009) suggest that LRGs and their host haloes have a typical misalignment angle of $\langle\theta_{mis}\rangle \sim 35°$. Their results strongly rejected a model in which the LRGs and the haloes are perfectly aligned. They model the misalignment distribution as a Gaussian with zero mean and a width of $\langle\theta_{mis}\rangle$. Okumura & Jing (2009) utilise this Gaussian misalignment distribution to model the GI correlation function of LRGs from SDSS. Based on these results, from both observations and simulations, we expect a significant amount of misalignment between the lens galaxies and their host haloes. For the rest of this section, we will discuss the implications of this misalignment.

We define a function $P(\theta_{mis})$ that represents the probability distribution of the misalignment angle between the galaxy light and the dark matter halo. This function is convolved with the angular parts of the anisotropic density distribution.

$$\Sigma(R,\theta) = \Sigma_0(R) + \Sigma_2(R)\cos(2\theta) \tag{3.26}$$

For this mass distribution we convolve $P(\theta)$ with $m_0(\theta) = 1$ and $m_2(\theta) = \cos(2\theta)$ to obtain a new mass distribution after stacking misaligned haloes.

$$\Sigma'(R,\theta) = \Sigma_0(R)m_0'(\theta) + \Sigma_2(R)m_2'(\theta) \tag{3.27}$$

In the equation above, $m_0'(\theta)$ and $m_2'(\theta)$ are the convolved angular functions.

The function $P(\theta_{mis})$ runs from $-\pi$ to π due to the symmetry of the system. A delta function centred on 0, $-\pi$, or π means the galaxy light is always oriented in the same

direction as the dark matter halo. The convolved dark matter distribution after stacking is the same as the true dark matter distribution. A constant $P(\theta_{mis})$ means there is no correlation between the alignment of the galaxy light and the alignment of the dark matter halo. This has the effect of completely circularising the lensing signal when the lenses are stacked.

A more reasonable probability distribution is a double-peaked Gaussian centred at 0, $-\pi$, and π. This means the light is often aligned with the dark matter halo, but there is a chance that it will be slightly misaligned depending on the width of the Gaussian peaks. This is a multi-peaked Gaussian because, due to symmetry, there is no difference between a misalignment angle of 0 or π. An example of this type of misalignment distribution is shown in Figure 3.3. The panel on the right shows the true matter distribution with a halo ellipticity of 0.4. The middle panel shows the probability distribution $P(\theta_{mis})$, in this case a double-peaked Gaussian. This Gaussian has a width of $\sigma = \pi/6$. This is about $30°$, close to the width of the Gaussian distribution of misalignment from Okumura et al. (2009). The left panel shows an example of the observed lensing signal after convolving with the probability distribution. This results in an observed matter distribution with an effective halo ellipticity of 0.23. This tells us that misalignment is degenerate with halo ellipticity. From observations, it is impossible to distinguish between inherent halo ellipticity and misalignment.

For our example of a Gaussian centred at 0 and π with a width of σ, we can calculate the analytic form for this misaligned mass distribution. The monopole angular function will be unchanged after the convolution, $m_0(\theta) = m_0'(\theta) = 1$. We can calculate the quadrupole angular function using the convolution theorem. By taking the Fourier transform of $\cos(2\theta)$ and $P(\theta)$, then by multiplying and taking the inverse transform of the result, we obtain $m_2'(\theta) = \exp(-2\sigma^2)\cos(2\theta)$. Our effective mass distribution, taking misalignment into account, is displayed on the right subplot of Figure 3.3. The quadrupole term of the effective mass distribution is $\Sigma_2(R)\exp(-2\sigma^2)\cos(2\theta)$, which is equivalent to $\Sigma_0(R)e\eta_0(R)\exp(-2\sigma^2)\cos(2\theta)$. The effect of this misalignment on the mass distribution is equivalent to a quadrupole term $\Sigma_0(R)e_{eff}\eta_0(R)\cos(2\theta)$ with an effective halo ellipticity of $e_{eff} = e \cdot \exp(-2\sigma^2)$.

3.4 Clampitt-Jain Estimators

The first of two sets of quadrupole estimators that we will use was developed by Clampitt & Jain (2016), and will be referred to as the Clampitt-Jain (CJ) estimators. The purpose
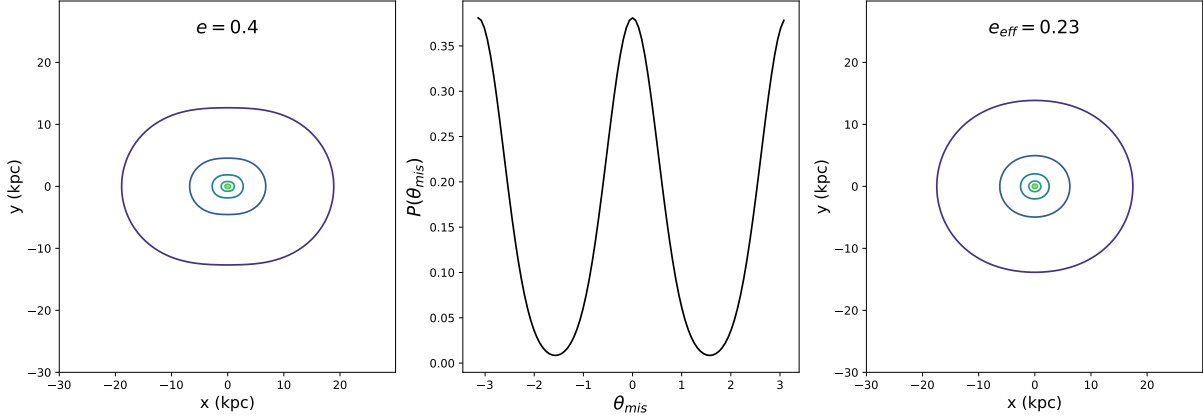
Figure 3.3: Misalignment between the galaxy light and the 1-halo dark matter term. The panel on the left shows the true matter distribution with a halo ellipticity of 0.4. The middle panel shows the probability distribution $P(\theta)$, in this case a double-peaked Gaussian. The right panel shows an example of the observed lensing signal after convolving with the probability distribution. This results in an observed matter distribution with an effective halo ellipticity of 0.23.

of these estimators is to maximise the quadrupole signal, while cancelling any contribution from the monopole shear.

A given source will have shape measurements (e_1, e_2). Each of these shape components will have a corresponding mass density. These mass densities will make use of the two functions $I_1(R)$ and $I_2(R)$.

$$I_1(R) = \frac{3}{R^4} \int_0^R R'^3 \Sigma_0(R') \eta_0(R') dR' \tag{3.28}$$

$$I_2(R) = \int_R^\infty \frac{\Sigma_0(R') \eta_0(R')}{R'} dR' \tag{3.29}$$

The estimators will make use of the shape measurements and Σ_{crit}. Adhikari et al. (2015) give these as

$$\Sigma_{crit} \gamma_1(R, \theta) = (\epsilon/4)[(2I_1(R) - \Sigma_0(R)\eta_0(R)) \cos 4\theta + 2I_2(R) - \Sigma_0(R)\eta(R)] \tag{3.30}$$

$$\Sigma_{crit} \gamma_2(R, \theta) = (\epsilon/4)[2I_1(R) - \Sigma_0(R)\eta_0(R)] \sin 4\theta \tag{3.31}$$

We will be using 4 estimators. The first pair of estimators, $\Delta\Sigma_1^{(+)}$ and $\Delta\Sigma_1^{(-)}$, will use the γ_1 shape measurement. The estimators will be either + or - depending on the sign of

$\cos(4\theta)$, which appears in Equation 3.30.

$$\Delta\Sigma_1^{(+)}(R) = \frac{4}{\pi} \int_{-\pi/8}^{\pi/8} \Sigma_{crit}\gamma_1(R,\theta)d\theta \tag{3.32}$$

$$\Delta\Sigma_1^{(-)}(R) = \frac{4}{\pi} \int_{\pi/8}^{3\pi/8} \Sigma_{crit}\gamma_1(R,\theta)d\theta \tag{3.33}$$

The final pair of estimators, $\Delta\Sigma_2^{(+)}$ and $\Delta\Sigma_2^{(-)}$, will use the γ_2 shape measurement. The sign of these estimators will depend on the sign of $\sin(4\theta)$ which appears in Equation 3.31.

$$\Delta\Sigma_2^{(+)}(R) = \frac{4}{\pi} \int_{0}^{\pi/4} \Sigma_{crit}\gamma_2(R,\theta)d\theta \tag{3.34}$$

$$\Delta\Sigma_2^{(-)}(R) = \frac{4}{\pi} \int_{\pi/4}^{\pi/2} \Sigma_{crit}\gamma_2(R,\theta)d\theta \tag{3.35}$$

In practice, these estimators will be calculated with a weighted average.

$$\Delta\Sigma_k^{(s)} = \frac{\sum w\Sigma_{crit}W_{crit}\gamma_k}{\sum wW_{crit}} \tag{3.36}$$

In the estimator, k refers to which ellipticity component (γ_k) is used in the weighted average. The angular range of the weighted average changes depending on k and s.

$$
\begin{aligned}
k = 1, s = + : \quad & -\pi/8 \leq \theta < \pi/8 \\
k = 1, s = - : \quad & \pi/8 \leq \theta < 3\pi/8 \\
k = 2, s = + : \quad & 0 \leq \theta < \pi/4 \\
k = 2, s = - : \quad & \pi/4 \leq \theta < \pi/2
\end{aligned} \tag{3.37}
$$

The uncertainty in this weighted average can also be calculated using Equation 3.4 as it was for the monopole. The only difference is the sums are calculated over specific angular ranges instead of for all sources.

To visualise the estimators, a diagram is displayed in Figure 3.4. This figure displays a lens, represented by an ellipse in the centre, that has been rotated to align with the x-axis. The sources are created as circles which experience a monopole shear in the top subplots or a quadrupole shear in the bottom subplots. Regions shaded in red are covered by the "+" estimators and regions shaded in blue are covered by the "-" estimators. The value of the CJ estimators are calculated using the mock sources. The value of these estimators
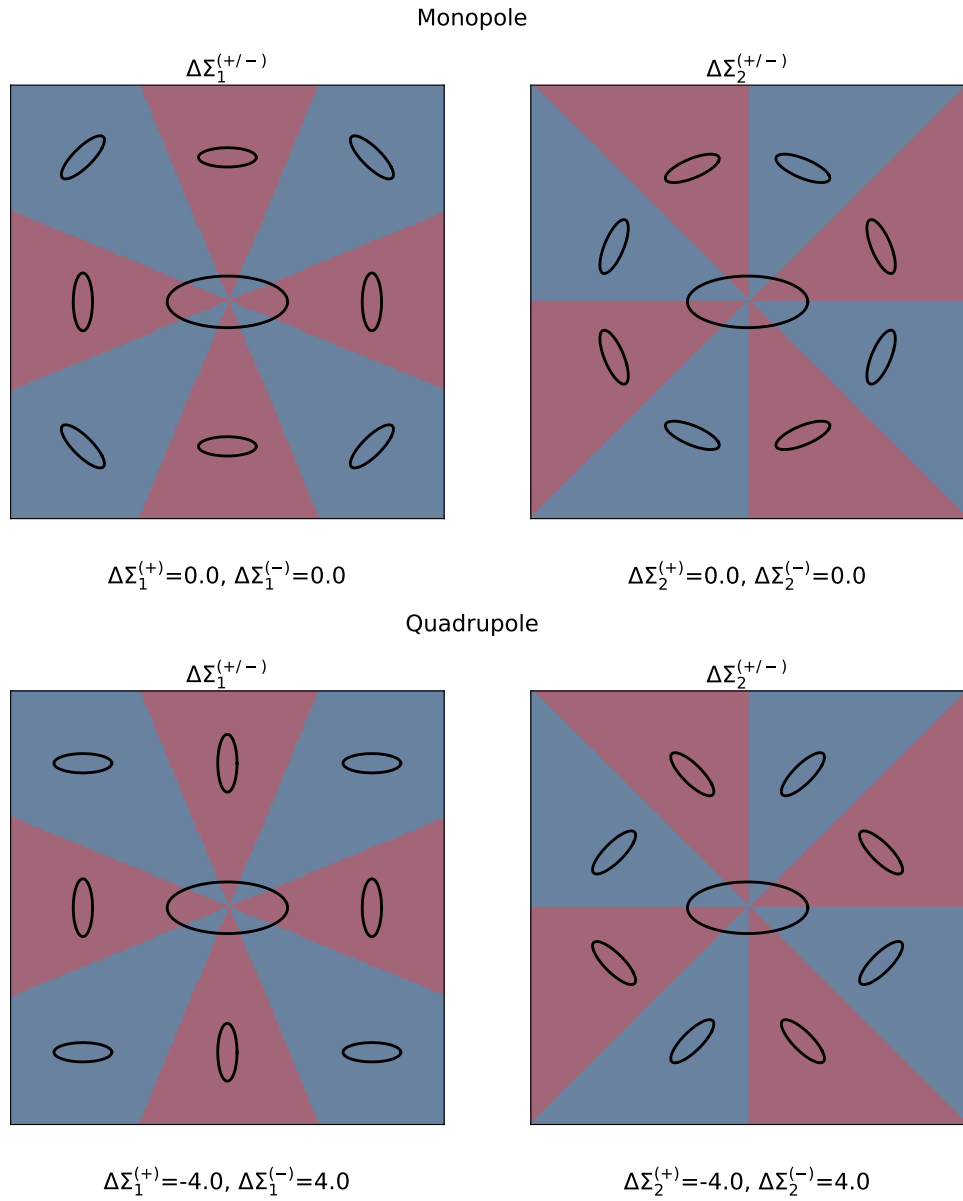
33

Figure 3.4: A visualisation of a lens aligned with the x-axis, with sheared sources represented as ellipses around the lens in the centre. The sources in the top subplots have a simulated monopole shear applied, while the sources in the bottom subplots have a simulated quadrupole shear. The left subplot describes the $\Delta\Sigma_1$ estimators, while the right subplot describes the $\Delta\Sigma_2$ estimators. Regions shaded in red are covered by the "+" estimators and regions shaded in blue are covered by the "-" estimators.

is displayed below the subplots. For the monopole, these estimators are 0, meaning any non-zero value is the result of quadrupole shear.

Taking the $\Delta\Sigma_1^{(+)}$ estimator in Figure 3.4 as an example, this estimator measures γ_1 in the red region in the left subplots. For the quadrupole shear we can see this includes four sources. The two sources along the major axis experience a tangential shear, while the two sources along the minor axis experience a radial shear. This is equivalent to all four sources having a negative γ_1 shape component. This negative γ_1 is added to the weighted average for all sources within this region. This yields the value of $\Delta\Sigma_1^{(+)} = -4.0$ that we see below the subplot.

By evaluating these integrals, we can derive equations for the model to fit to the data from the weighted averages. These are

$$\Delta\Sigma_1^{(+)} = \frac{e}{2\pi} \left[2I_1(R) - \Sigma_0(R)\eta_0(R)\right] + \frac{e}{4}2I_2(R) - \frac{e}{4}\Sigma_0(R)\eta(R) \tag{3.38}$$

$$\Delta\Sigma_1^{(-)} = -\frac{e}{2\pi} \left[2I_1(R) - \Sigma_0(R)\eta_0(R))\right] + \frac{e}{4}2I_2(R) - \frac{e}{4}\Sigma_0(R)\eta(R) \tag{3.39}$$

$$\Delta\Sigma_2^{(+)} = \frac{e}{2\pi} \left[2I_1(R) - \Sigma_0(R)\eta_0(R)\right] \tag{3.40}$$

$$\Delta\Sigma_2^{(-)} = -\frac{e}{2\pi} \left[2I_1(R) - \Sigma_0(R)\eta_0(R)\right] \tag{3.41}$$

3.5 Natarajan-Refregier Estimators

In this section, we will discuss an alternate set of estimators for the quadrupole shear. The formalism for these estimators was developed by Natarajan & Refregier (2000), and the estimators would go on to be further developed by several other groups (Mandelbaum et al., 2006c; Schrabback et al., 2015). These estimators will be referred to as the Natarajan-Refregier (NR) estimators. The mass density model used for these estimators is similar to the one described in Equation 1.8.

$$\Delta\Sigma(r) = \Delta\Sigma_{iso}(r) \left[1 + 2f(r)e_g \cos(2\theta)\right] \tag{3.42}$$

This yields two estimators, $f\Delta\Sigma$ and $f_{45}\Delta\Sigma$, that depend on the tangential and cross shear components (e_t and $e_\times$).

$$f(r)\Delta\Sigma(r) = \frac{\sum_i w_i \Sigma_{crit}^{-1} |e_{g,i}| e_{t,i} \cos(2\theta_i)}{2 \sum_i w_i \Sigma_{crit}^{-2} |e_{g,i}|^2 \cos^2(2\theta_i)} \tag{3.43}$$
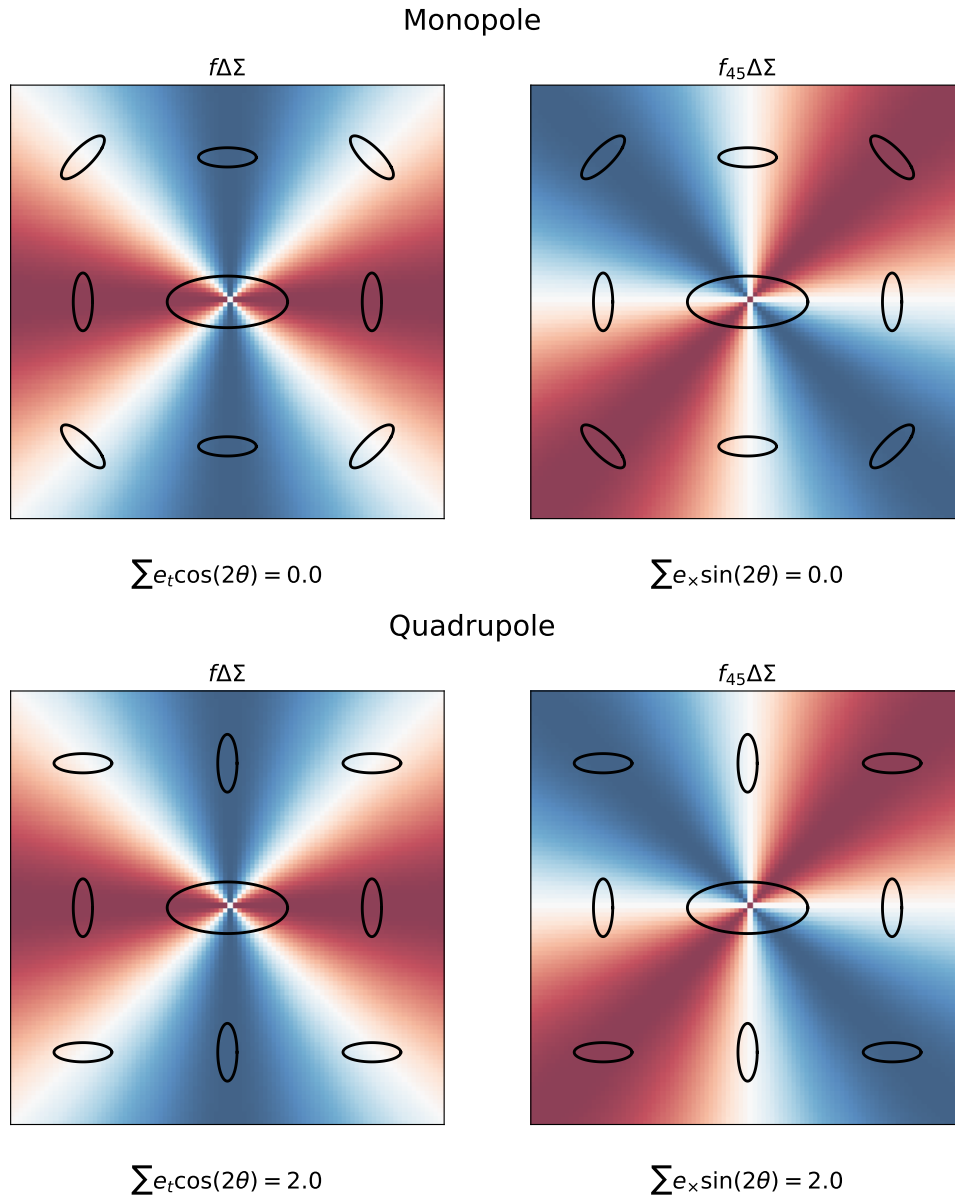
Figure 3.5: A visualization of the NR estimators. The lens is the ellipse at the centre of each subplot. Sources are represented by ellipses surrounding the lens. The sources experience a monopole shear in the top subplots and a quadrupole shear in the bottom subplots. The weighting functions $\cos(2\theta)$ and $\sin(2\theta)$ are displayed in the background on the left and right respectively. The plot is coloured red where the functions are positive and blue where they are negative. The results of the estimators are displayed below each subplot.

$$f_{45}(r)\Delta\Sigma(r) = \frac{\sum_i w_i \Sigma_{crit}^{-1} |e_{g,i}| e_{\times,i} \sin(2\theta_i)}{2 \sum_i w_i \Sigma_{crit}^{-2} |e_{g,i}|^2 \sin^2(2\theta_i)} \tag{3.44}$$

It is worth noting that the sign convention for the shears are different than for the CJ estimators. For example, a source at an angle of $\theta = 0$ experiencing a purely vertical shear would have a negative e_1 ellipticity component. However, this would be a positive tangential shear, or a positive e_t ellipticity component. The uncertainty for the tangential estimator is

$$\sigma(R) = \frac{\sqrt{\sum (\Sigma_{crit} W_{crit} \sigma_e w \cos 2\theta)^2}}{2 \sum W_{crit} w \cos^2(2\theta)} \tag{3.45}$$

and for the cross estimator

$$\sigma(R) = \frac{\sqrt{\sum (\Sigma_{crit} W_{crit} \sigma_e w \sin 2\theta)^2}}{2 \sum W_{crit} w \sin^2(2\theta)} \tag{3.46}$$

A visualisation of these estimators is visible in Figure 3.5. A single lens system was created and rotated to align the major axis of the lens with the x-axis. The lens appears as an ellipse in the centre of the subplots. Sources are represented as ellipses around the lens. The sources experience a monopole shear in the top subplots and a quadrupole shear in the bottom subplots. The tangential and cross shear of the sources are used to calculate the estimators in Equations 3.43 and 3.44. The weighting functions $\cos(2\theta)$ and $\sin(2\theta)$ are displayed in the background on the left and right respectively. The plot is coloured red where the functions are positive and blue where they are negative. Below the plots are the results of each the estimators. As we saw with the CJ estimators, monopole shear yields a value of 0 and any non-zero value is the result of quadrupole shear.

As an example, the $f\Delta\Sigma$ estimator in Figure 3.5 measures the tangential shear of the sources in the left subplots and weights them with $\cos(2\theta)$. The two sources along the major axis experience a tangential shear, which is weighted positively. The two sources along the minor axis experience a radial shear, which is equivalent to a negative tangential shear. This radial shear is weighted negatively by the weighting function. The four sources along the diagonal are in areas where $\cos(2\theta) = 0$, and do not contribute to the weighted average. The combination of the tangential and radial shears yield the value for the weighted average that we see below the subplot.

We can derive the model, the integral forms of these weighted averages, in the same manner as what was done for the CJ estimators. Clampitt & Jain (2016) give

$$\Sigma_{crit}\gamma_t = (e/2)[\Sigma_0(R)\eta_0(R) - I_1(R) - I_2(R)] \cos 2\theta \tag{3.47}$$

$$\Sigma_{crit}\gamma_\times = (e/2)[-I_1(R) + I_2(R)] \sin 2\theta \tag{3.48}$$

37

using $I_1(R)$ and $I_2(R)$ defined in the previous section. If we assume a scenario where every source is equally weighted, and the same Σ_{crit} is used for every source around a given lens, the weighted averages simplify. We can then covert these weighted averages to integral form.

$$f(r)\Delta\Sigma(r) = \frac{\int (e/2)[\Sigma_0(R)\eta_0(R) - I_1(R) - I_2(R)]e_g \cos^2 2\theta}{2\int \cos^2 2\theta} \tag{3.49}$$

$$f_{45}(r)\Delta\Sigma(r) = \frac{\int (e/2)[-I_1(R) + I_2(R)]e_g \sin^2 2\theta}{2\int \sin^2 2\theta} \tag{3.50}$$

The only θ dependence is in the $\cos^2(2\theta)$ and $\sin^2(2\theta)$ terms, which cancel out. These estimators simplify to

$$f(r)\Delta\Sigma(r) = \frac{e}{4}e_g[\Sigma_0(R)\eta_0(R) - I_1(R) - I_2(R)] \tag{3.51}$$

$$f_{45}(r)\Delta\Sigma(r) = \frac{e}{4}e_g[-I_1(R) + I_2(R)] \tag{3.52}$$

3.6   Mock Source Catalogue

In order to describe the results we expect to observe from the quadrupole estimators, we construct an idealized mock source catalogue. The purpose of the mock source catalogue described in this section is to visualise the results we expect from the estimators, and not to estimate the feasibility of measuring halo ellipticity using these estimators. The mock catalogue consists of a grid of sources around a single lens with a given lens light angle. These sources are initially circles, and hence have no shape noise, which then experience an ideal monopole and quadrupole shear from the model.

The shears each source experience are a combination of monopole and quadrupole shear. The monopole shears do not depend on lens alignment. For a given lens model they are calculated by

$$\gamma_{1M}(r) = -\frac{\Delta\Sigma(r)}{\Sigma_{crit}} \cos(2\theta) \tag{3.53}$$

$$\gamma_{2M}(r) = -\frac{\Delta\Sigma(r)}{\Sigma_{crit}} \sin(2\theta) \tag{3.54}$$

The quadrupole shears are calculated using Equation 3.30 and Equation 3.31, then dividing by Σ_{crit}. This will yield quadrupole shear coordinates γ_{1Q} and γ_{2Q}. The total shears are then calculated using $\gamma_1 = \gamma_{1M} + \gamma_{1Q}$. These total shears can be generated
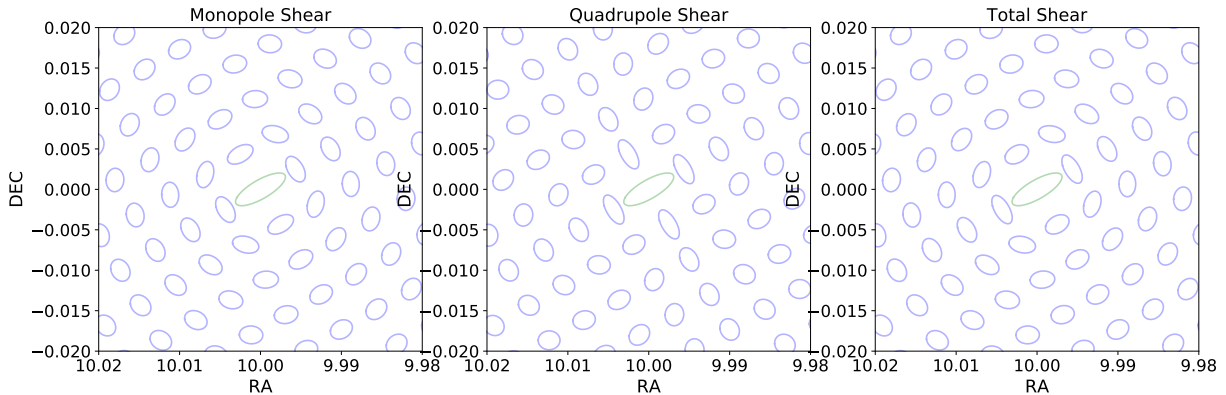
Figure 3.6: A mock single-lens system with a grid of sources. The lens is at the centre in green and the sources are in blue. The left subplot displays the monopole shear, the centre subplot displays the quadrupole shear, and the right subplot displays the total shear. These shears are multiplied by a constant factor in order to make the shapes more distinguishable. This particular system has a lens position angle of 30 °.

and combined into a catalogue of sources that is similar in format to the CFIS data. The process of stacking the shear and applying the quadrupole estimators can then be applied.

An example of a mock single-lens system is visible in Figure 3.6. The monopole shear, quadrupole shear, and total shear are all separately displayed. These shears are multiplied by a constant factor in order to make the shapes more distinguishable. This particular system has a lens position angle of 30 °. The sources are originally generated in a coordinate system aligned with the x-axis. To generate a system with a non-zero lens position angle, the sources are then rotated by the desired angle using the process described previously.

The results of applying the quadrupole lensing method to our mock source catalogue are visible in Figure 3.7. The plots on the left and centre are for the CJ estimators and the plots on the right are for the NR estimators. Models for the estimators are described in Sections 3.4 and 3.5. The data and the models were generated for an elliptical halo with mass $M_{200} = 10^{13} M_\odot$ and an ellipticity of $e = 0.4$.

In order to visualise the elliptical mass distribution, we can plot the shear and convergence as a 2D map. This is done by aligning the lens major axis with the x-axis, and then binning the shear into 2D bins. For each 2D bin, we plot a stick which has a size and direction determined by the result of the weighted average for e_1 and e_2 in that bin. The magnitude is

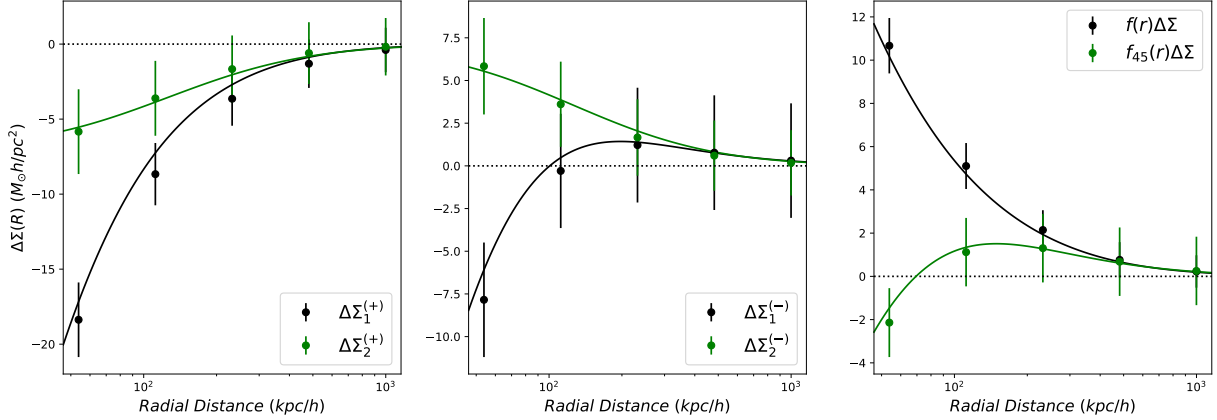$$e = \sqrt{e_1^2 + e_2^2} \tag{3.55}$$

39

Figure 3.7: Results from a mock single-lens system. The left and centre subplots contain the CJ estimators, the right subplot displays the NR estimators. Models for the estimators are described in the Sections 3.4 and 3.5. Data and models were generated with for an elliptical halo of mass $M_{200} = 10^{13} M_\odot$ and an ellipticity of $e = 0.4$.

and the direction is defined by an angle $\theta = \frac{1}{2}\arctan(e_2/e_1)$. The coordinates of the endpoints of the stick are $(-\frac{e}{2}\cos\theta, -\frac{e}{2}\sin\theta)$ and $(\frac{e}{2}\cos\theta, \frac{e}{2}\sin\theta)$. This is repeated for every bin to generate a 2D shear map.

The results for the shear map are displayed in Figure 3.8. The top left displays total shear. The top right displays the monopole fit after re-binning into radial bins. The bottom left displays the expected 2D monopole shear. The bottom right displays the residual shear. We can see that after subtracting the monopole shear the result is a clear quadrupole shear pattern.

It may be difficult to interpret the results from the stickplot. We use the method described by Kaiser & Squires (1993) and Kaiser et al. (1995) to convert this shear map into a convergence map. The convergence is directly proportional to the projected mass density, which may make it easier to visualise the elliptical mass distribution. The mock convergence map is displayed in Figure 3.9. The left subplot displays the total shear. The projected density is that of an elliptical dark matter halo. The centre subplot displays the result of the monopole fit. The right subplot displays the residual shear. After subtracting the monopole, we are left with the mass density of the quadrupole shear. As expected, there is an excess of mass along the major axis and a deficit along the minor axis.
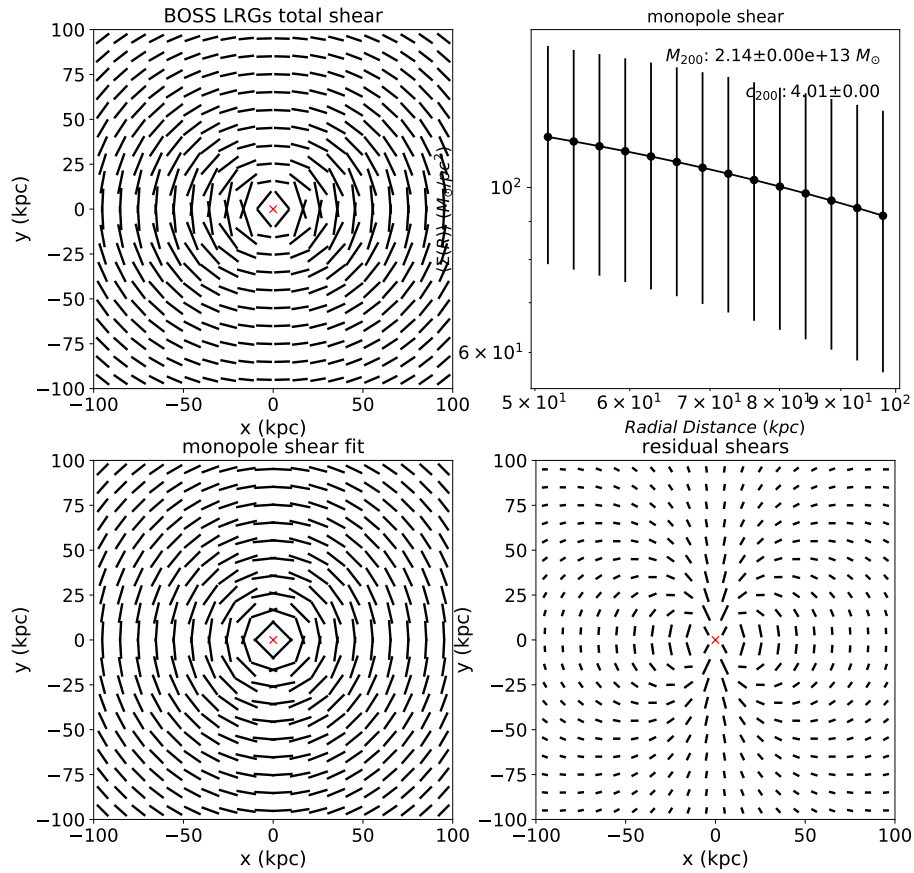
Figure 3.8: Shear map for mock single-lens system. The top left displays total shear. The top right displays the monopole fit after re-binning into radial bins. The bottom left displays the expected 2D monopole shear. The bottom right displays the residual shear.
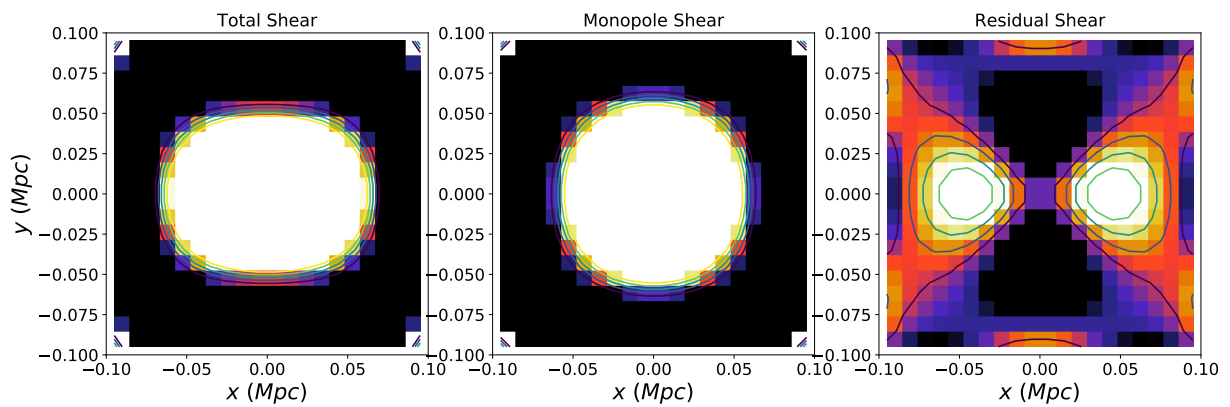
Figure 3.9: Convergence map for mock single-lens system. The left subplot displays the total shear. The centre subplot displays the result of the monopole fit. The right subplot displays the residual shear.

Chapter 4

Results

In this chapter, we will discuss the results of the shear measurements. First, we will explore the monopole shear and its NFW profile fit, as well as the quadrupole shear. We will also discuss the process used to account for systematic effects. We will then examine possible sources of bias and how they may affect our results. Finally, we will compare to results using the SDSS light angles.

4.1 Monopole Shear

Before we can fit the elliptical model to the quadrupole shear, we first fit the isotropic model to the monopole shear. The monopole shear was calculated in radial bins and an NFW profile was fit with halo mass and concentration as free parameters. Only bins within 1 Mpc/h from the centre of the lens were included in the fit, as beyond this radius effects from other haloes and surrounding structures become significant.

The results of the stacking and the fit are visible in Figure 4.1. The halo mass and concentration from the fit, as well as their uncertainties, are displayed in the upper right corner of the plot. Both parameters are quite well constrained, and there is good agreement between the inner bins and the model. From the monopole fit, we obtain a halo mass of $M_{200} = 1.24 \pm 0.05 \times 10^{13} M_\odot$ and a concentration of $c_{200} = 2.06 \pm 0.16$. This is smaller than the concentration predicted by mass-concentration relations. For a halo of this mass, Duffy et al. (2008) predict a concentration $c_{200} \sim 4$, while Dutton & Macciò (2014) predict $c_{200} \sim 5$. Our model consists of only a 1-halo term. In reality, some of the LRGs will be satellites inside of a larger halo. This is normally described by the inclusion
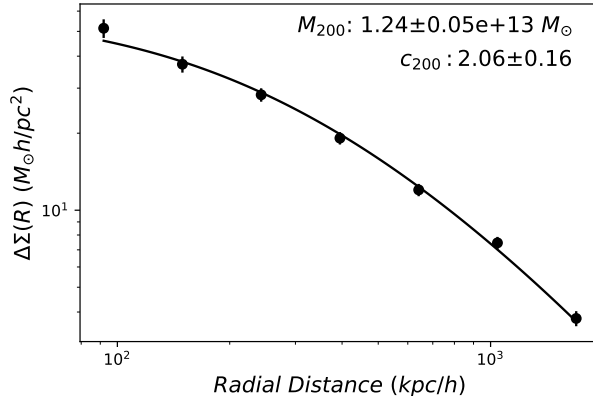
Figure 4.1: Results for the monopole shear. Only bins within 1 Mpc/h were included in the fit. The halo mass and concentration are displayed in the plot.

of an offset group term. Neighbouring halos will also contribute to the lensing signal, which can be described by a 2-halo term. These terms are not included in the model, so it is not meaningful to compare to standard mass-concentration relations. If we were to include these terms, we would measure a different mass and concentration. Regardless, the model fits the data well, which is all that is necessary in order to extract the ellipticity.

4.2 Quadrupole Shear

Results for the quadrupole shear are displayed in Figure 4.2. The results for the CJ estimators are visible in the left and centre subplots, while the results for the NR estimators are visible on the right. An elliptical model was fit to each of the 6 quadrupole estimators separately. This model used the halo mass and concentration from the monopole fit, with only e as a free parameter. Only radial bins within 600 kpc/h were included in the fit, as surrounding structure contributes a significant amount of anisotropy at high radius. The region included in the fit is plotted with a solid line, while the region outside the fit is plotted with a dashed line. All estimators are calculated within the same radial bins. However, for visualisation purposes, points plotted in green have been shifted to the right. The best fit of e for each estimator is displayed in each subplot.

Most of the measurements from each of the 6 estimators are consistent with zero. However, there are two measurements which suggest halo ellipticity. Both $\Delta\Sigma_1^{(+)}$ and $f\Delta\Sigma$ yield positive ellipticities. We can quantify the significance of the agreement between
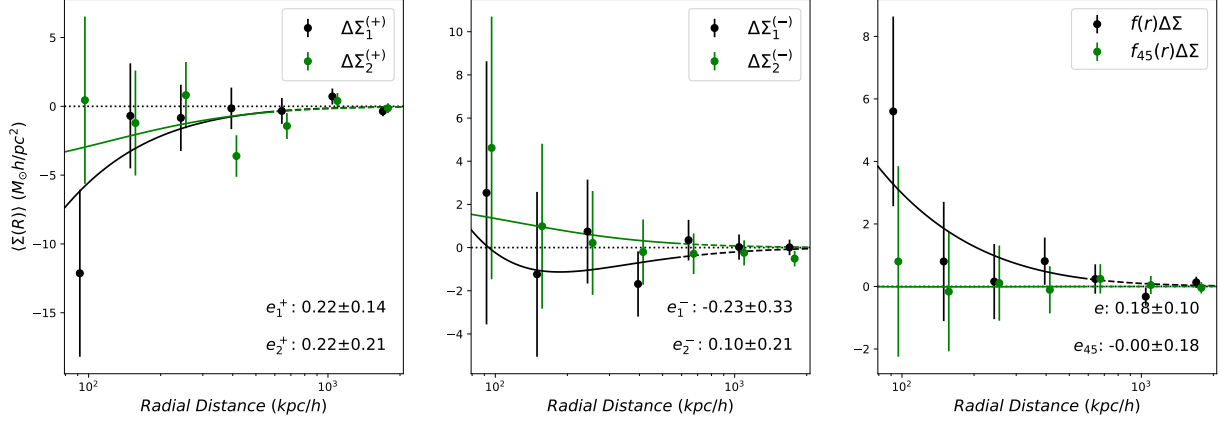
44

Figure 4.2: Quadrupole shear for LRGs using light angles from CFIS. The left and centre subplots display the results for the CJ estimators, while the right subplot is for the NR estimators. A model has been fit to the data. The fit was only performed using points within 600 kpc/h of the centre of the lens. The region included in the fit is plotted with a solid line, while the region outside the fit is plotted with a dashed line. Points plotted in green have been shifted to the right. The best fit of e for each estimator is displayed in each subplot.
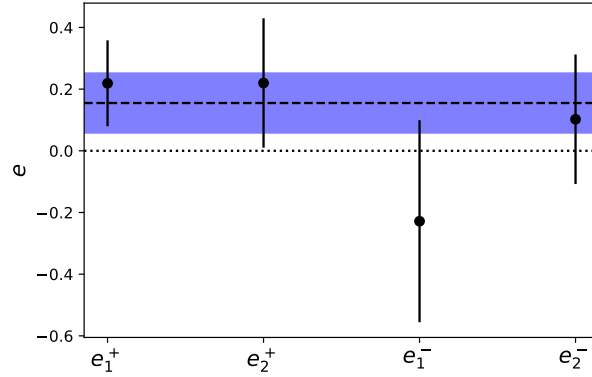

Figure 4.3: Halo ellipticity values from fits to the 4 CJ estimators and their uncertainties using light angles from CFIS. The weighted average halo ellipticity ($e = 0.155$) is plotted as a dashed black line. The range of 1σ uncertainty in the mean is shaded in blue ($\Delta e = 0.097$). No ellipticity is represented with a dotted black line at $e = 0$.

45

the ellipticity values from the fits. A weighted average of the halo ellipticity is taken using the uncertainty in the value of e from the fit ($w = \sigma^2$). The 4 ellipticities from the CJ estimators are independent of each other, covering different angular ranges around the lens. However, these estimators are not independent of the 2 NR estimators. For this weighted average, only the 4 CJ estimators are used. From the 4 CJ estimators, the mean halo ellipticity is $e = 0.155 \pm 0.097$. If we assume these 4 values of ellipticity are fit with a constant, we can calculate the χ^2 of this hypothetical fit with the mean e as the constant. We have 3 degrees of freedom (4 values of e and 1 constant parameter).

$$\chi_\nu^2 = \frac{1}{\nu} \sum_i \frac{(e_{obs,i} - \bar{e})^2}{\sigma_{e,i}^2} \tag{4.1}$$

We can visualise the constant model and the data in Figure 4.3. The values of e from each of the 4 CJ fits are the data we wish to fit with the constant model. The χ_ν^2 is a measure of how well this constant model fits that data. A value of $\chi_\nu^2 \sim 1$ is ideal, and indicates that deviation among the measurements is within an acceptable range. A value $\chi_\nu^2 \gg 1$ indicates that the model does not adequately describe the variation in the data. In this case, we calculate a value of $\chi_\nu^2 = 0.58$. This value is less than 1, indicating the 4 CJ measurements are consistent with a constant model. Although this value is less than 1, it is not lower than expected. The probability density function for the χ^2 distribution depends on the number of degrees of freedom. Evaluating the cumulative distribution function for a χ^2 with 3 degrees of freedom yields a probability of 37% that $\chi_\nu^2 \leq 0.58$.

We can also visualise these results using the 2D shear and convergence maps discussed previously. We calculated the 2D shear in a 30x30 grid that spans -3 Mpc to 3 Mpc in both dimensions. However, as a result of binning sources in 2D, sources that are extremely close to the lens are included. Light from the lens contaminates sources that are too close, leading to an inaccurate shape measurement. In order to account for this, no sources within 25 kpc were included in any of the 2D bins. We rebinned the 2D bins into radial bins. A monopole model was fit to the average shear as a function of these radial bins. This monopole was then used to generate the expected monopole shear for each 2D bin. The monopole shear was then subtracted from the data to obtain the residual shear. If there is a significant quadrupole, we should expect to see it in the residuals. We can then use the shear map to calculate the convergence map.

The result of this process is displayed in Figure 4.4. On the left is the convergence from the data after correcting the inner bins. In the centre is the result of the monopole fit. On the right are the results from the residuals after subtracting the monopole shear. In the left subplot, we expect to see an elliptical halo with a major axis along the x-axis.
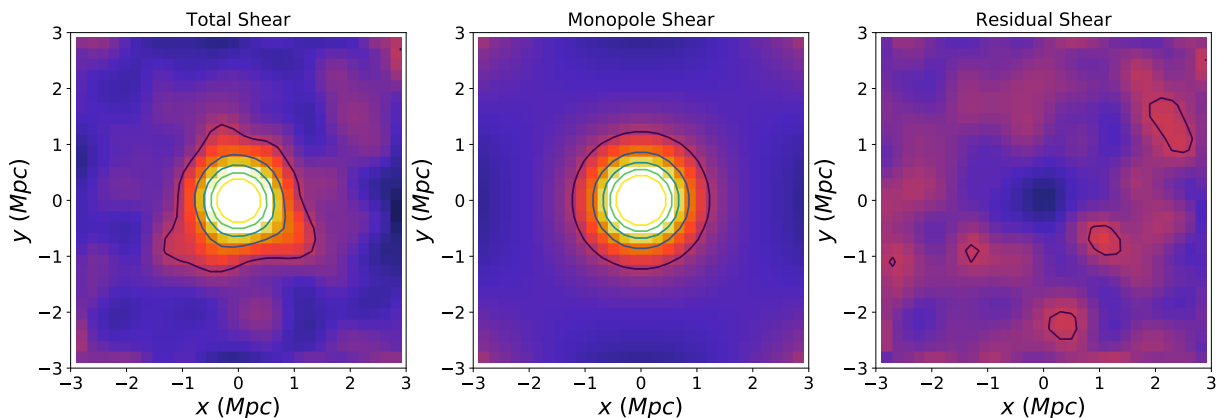
Figure 4.4: Results of applying the KSB algorithm to the shear map. On the left is the convergence from the data. In the centre is the result of the monopole fit. On the right are the results from the residuals after subtracting the monopole shear.

However, the density distribution appears to be round. In addition to this, there should be evidence of the quadrupole in the right subplot, which we do not see.

One possible reason for the apparent lack of ellipticity in the convergence maps is due to the how the sources are binned in 2D. The accuracy of weak lensing as a technique increases as we increase the number of sources in the weighted average. The quadrupole estimators are effective because they allow us to study azimuthal variation in the shear without splitting the sources into several separate weighted averages. However, in the convergence map the sources are binned in 2D and are distributed into many more bins. Each weighted average will have fewer sources and a less accurate measurement of shear. Additionally, unlike for the quadrupole estimators, we have not applied systematic corrections to the convergence map. There is an unexpected area of low density in the center of the right subplot of Figure 4.4. This is likely due to how we have extrapolated the monopole. As discussed previously, the concentration from the monopole is different than predictions from standard mass-concentration relations. The inner regions of the convergence map may not be well represented by the model.

4.3 Systematic Effects

It is possible that there are systematic effects in the shape measurements that may affect our results. We can study any potential biases by creating a catalogue of random lenses.
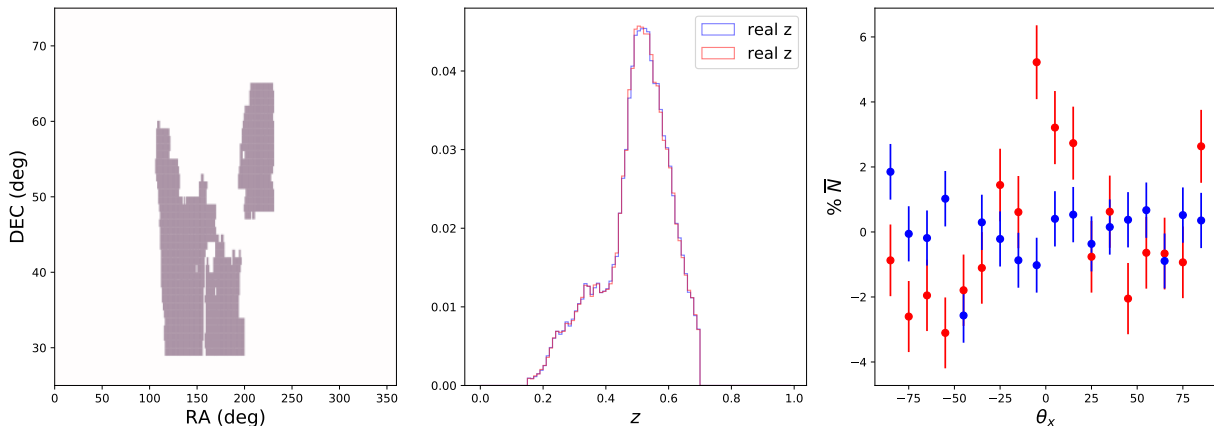
47

Figure 4.5: A comparison of the BOSS LRG data and the simulated random lens catalogue. Information pertaining to the real data is plotted in red and for the random lenses, in blue. Left: distribution on the sky. Centre: redshift histogram. Right: position angle histogram.

These lenses will have randomly assigned RA, DEC, z, and θ_x. Lenses are assigned RA and DEC in a way that ensures a uniform distribution across the sky. The CFIS footprint is split into $0.5° \times 0.5°$ regions. Each lens is randomly assigned a region. For each region, all lenses are assigned a right ascension by drawing uniformly from within the range RA_{left} to RA_{right}, which are the boundaries of the region. All lenses are also assigned a declination by drawing uniformly from $\sin(\text{DEC}_{lower})$ to $\sin(\text{DEC}_{upper})$ and taking the arcsin of the results. The distributions of lenses on the sky for both the BOSS LRG data and the simulated lens catalogue are shown in the left subplot of Figure 4.5. For all subplots of this figure, information pertaining to the real data is plotted in red and for the random lenses, in blue.

The redshifts are assigned in a way that attempts to represent the actual redshift distribution of the lens sample. Redshifts are randomly drawn from the redshifts of the LRG sample. This is repeated until the desired number of redshifts have been drawn. Histograms of the redshifts for the real and simulated lenses are shown in the central subplot of Figure 4.5. Finally, lens position angles are drawn uniformly from $-\pi/2$ to $\pi/2$. Histograms of lens position angles for real and random lenses are visible in the right subplot of Figure 4.5.

This process was used to generate a catalogue of 1,500,000 random lenses. The monopole shear was calculated using these lenses. In the absence of systematic effects, we would expect the monopole shear to be consistent with zero. Any signal we observe is the result of systematic effects. We can see the results of stacking the monopole shear for these ran-
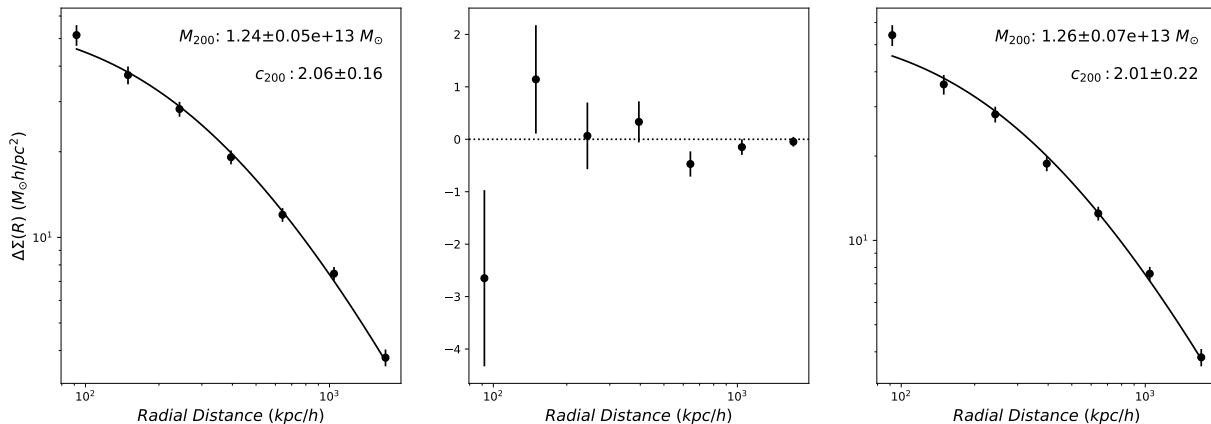
Figure 4.6: Results for the monopole shear. Left: observed monopole shear before accounting for systematic effects. Centre: results from random lenses used to visualise systematic effects. Right: monopole shear after subtracting systematics.

dom lenses in the centre subplot of Figure 4.6. For most radii, the systematic effects are consistent with zero.

The right subplot of Figure 4.6 displays the results of the monopole shear after subtracting the systematic shear (centre) from the observed shear (left). As expected, the density in most radial bins has changed little and is still consistent with the model. The innermost bin has been corrected for radial contamination, but this has not had much of an effect on the fit. The isotropic NFW model was once again fit to the corrected monopole shear. This yielded a halo mass of $M_{200} = 1.26 \pm 0.07 \times 10^{13}$ M$_\odot$ and a concentration of $c_{200} = 2.01 \pm 0.22$. The halo mass and concentration from the fit are displayed in the upper right corner. There are slight differences between the fit parameters before and after correcting for systematic effects. However, these differences are within the range of expected uncertainty for these parameters.

It is also possible that systematic effects could affect the quadrupole shear measurements. The same catalogue of 1,500,000 random lenses was used to calculate quadrupole shear and correct for systematic effects. The results of this correction on estimators calculated using CFIS light angles are displayed in Figure 4.7. Each row displays a different set of estimators: monopole, positive CJ, negative CJ, and NR estimators. The left column displays the results from stacking before any subtraction, while the right column displays results after subtracting the random results. Using the halo mass and concentration from the corrected monopole fit, elliptical models were fit to each estimator before and after the systematic correction. The results of measuring the quadrupole shear for the random

49
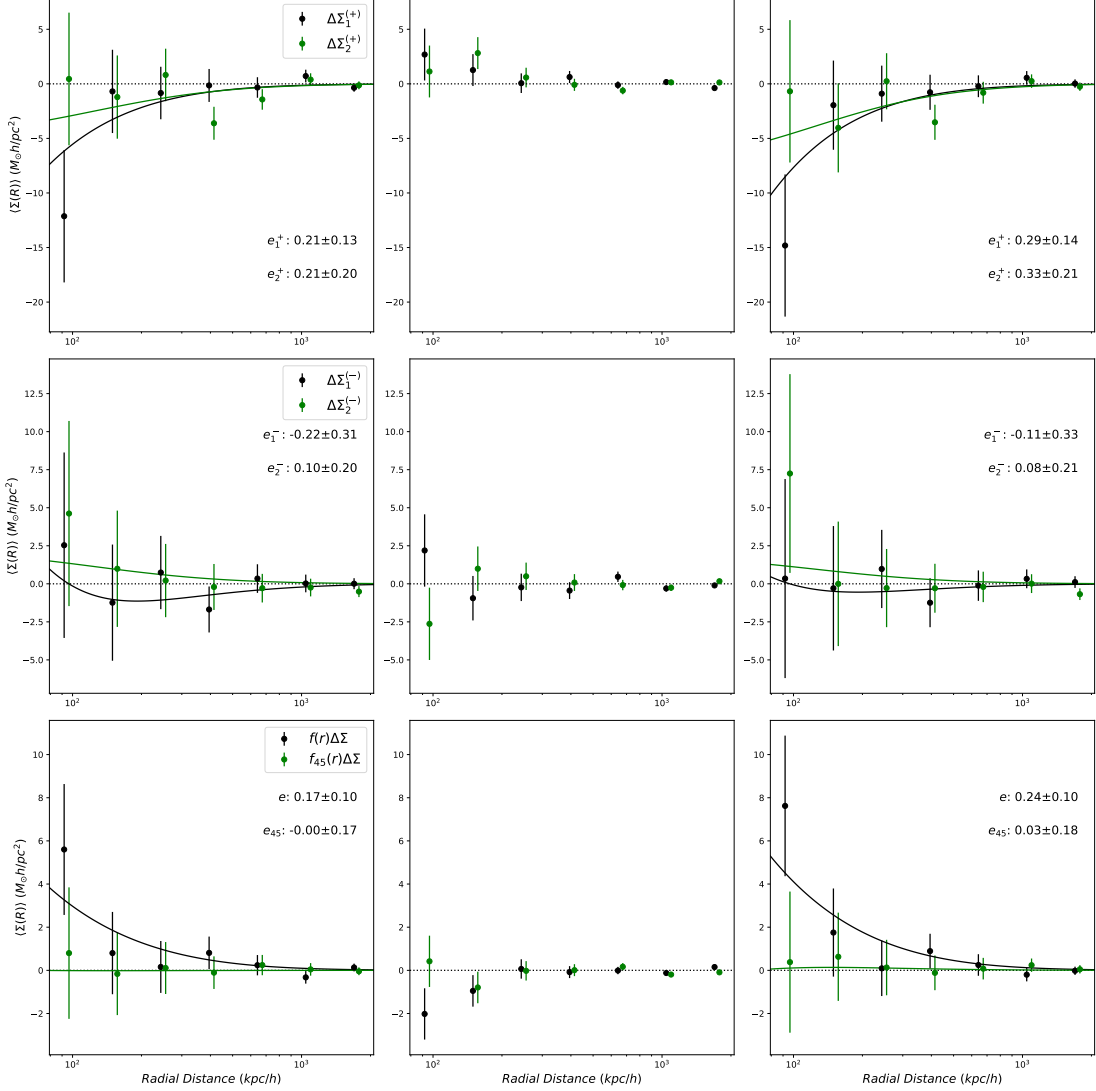
Figure 4.7: Projected mass density for all quadrupole estimators calculated using CFIS light angles.. Each row is for a different set of estimators: monopole, positive CJ, negative CJ, and NR estimators. The left column displays the results from stacking before any subtraction. The middle column are results calculated using the simulated random lenses as described in Section 4.3. The right column are results after subtracting the random results.
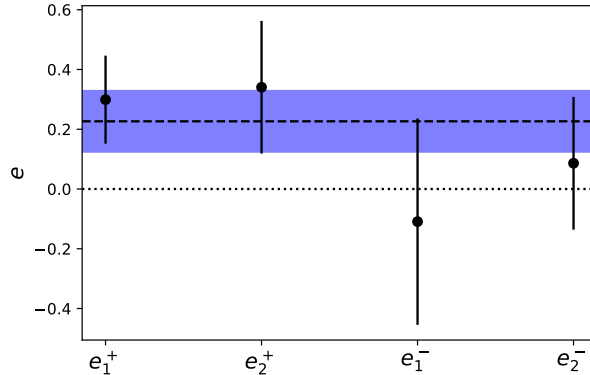
50

Figure 4.8: Halo ellipticity values calculated using the CFIS light angles, after accounting for systematic effects. Results are presented in the same format as Figure 4.3.

lenses (middle) are consistent with zero at most radii. The values of e are different before and after the correction, although the value of e does not change by more than the range of uncertainty for any of the estimators. In some cases, accounting for these systematic effects increases the value of the halo ellipticity from the fit.

We can repeat the process of calculating mean halo ellipticity and χ^2_ν for the values of ellipticity we obtain after correcting for systematic effects. We obtain a mean halo ellipticity of $e = 0.226 \pm 0.102$ and $\chi^2_\nu = 0.62$. A visualisation of the values of halo ellipticity from the fit, as well as the mean halo ellipticity, is shown in Figure 4.8.

Hereafter, we will use this process of subtracting the results from random lenses to account for systematic effects. The monopole shear will be calculated, then the results for the 1,500,000 random lenses will be subtracted. The subtracted results will then be fit by an NFW profile with halo mass and concentration as free parameters. The halo mass and concentration from the subtracted results will then be used to fit the elliptical model to the corrected quadrupole estimators.

4.4   Lens Shape Bias

It is possible that cosmic shear or the PSF could be affecting the shape measurements of the lens galaxies. This bias may affect both the lenses and the sources in a similar way, which could lead to correlations in the shape measurements. If this effect is significant enough, it could affect the measurement of halo ellipticity. Galaxies that already have
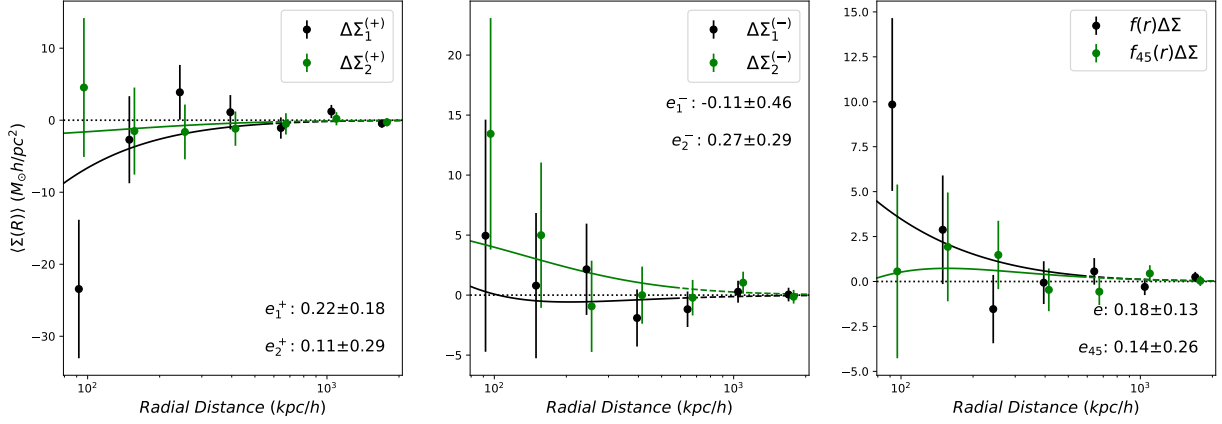
Figure 4.9: Results for quadrupole shear presented in the same format as Figure 4.2. Galaxies that are rounder than $e = 0.11172$ were removed from the sample.

a distinct shape will not be affected very much, but rounder galaxies may experience a significant change in their lens major axis angle. In order to test this effect, all galaxies that are rounder than the median ellipticity are eliminated from the lens sample before stacking.

The ellipticity was calculated for each lens using $e = (a-b)/(a+b)$ and the median was found to be $e = 0.11172$. All lenses rounder than this value were removed from the sample, leaving 73,000 lenses, and the quadrupole was calculated using both sets of estimators. The results are shown in Figure 4.9. The halo ellipticity was fit for each estimator and a weighted average was taken. The mean ellipticity is $e = 0.181 \pm 0.130$. The reduced $\chi_\nu^2 = 0.20$. This value is quite low, but calculating the cumulative distribution function for a χ^2 with 3 degrees of freedom reveals a 10% chance for $\chi_\nu^2 \leq 0.20$. This probability is not low enough to consider this to be a significant deviation. Although we have obtained a positive measurement of halo ellipticity, the uncertainty is much larger. This is due to stacking a lower number of lenses. Only half of the 146,000 lenses are included in the weighted average, which has led to a more inaccurate measurement of halo ellipticity.

Another way to avoid PSF issues in the shape measurement is calculate the angle from the ShapePipe measurements, which have been corrected for the PSF. The shape measurements, e_1 and e_2, can be used to calculate the position angle of the lens $\theta = \frac{1}{2}\arctan(e_2/e_1)$. However, some of the lenses are too bright or too large to be well fit by ShapePipe. Only 58,000 LRGs in our sample have well defined ellipticity coordinates. The results from these calculated angles are displayed in Figure 4.10. The mean halo ellipticity is $e = -0.077 \pm 0.191$ and $\chi_\nu^2 = 0.57$. This measurement of halo ellipticity is much
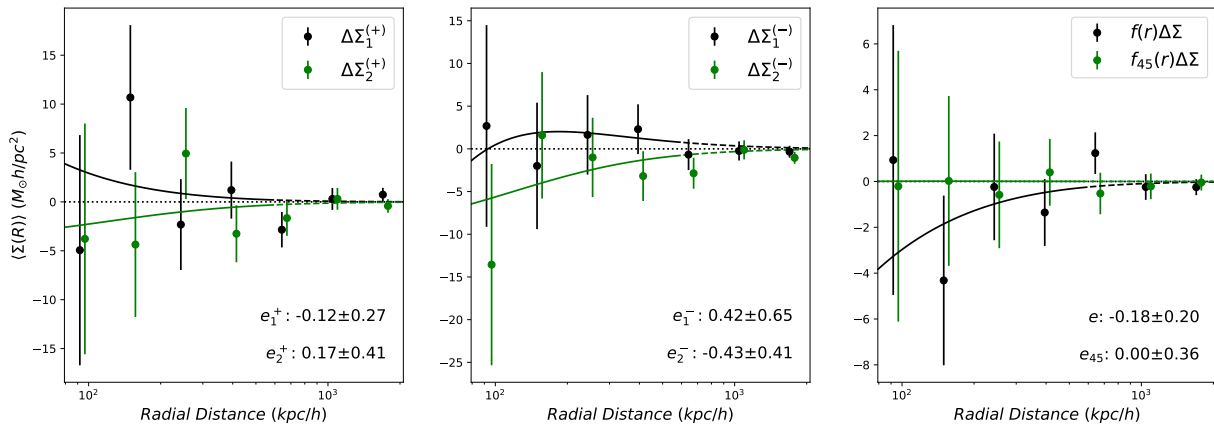
Figure 4.10: Results for quadrupole shear presented in the same format as Figure 4.2. Rather than using the angle from SExtractor, angles are calculated using $\theta = \frac{1}{2}\arctan(e_2/e_1)$. There are only about 58,000 LRGs that have well defined e_1's and e_2's, as opposed to the 150,000 LRGs normally used.

different from the value previously measured. Once again, this is likely due to a lower number of lenses. To obtain this measurement, we required lenses with well defined e_1 and e_2 from ShapePipe. Only 58,000 lenses, about a third of our lens sample, met this requirement. The lower number of lenses in the weighted average has led to a less accurate measurement of halo ellipticity.

4.5   Major Axis from SDSS

Results for the quadrupole shear using the SDSS lens position angle are displayed in Figure 4.11. Similar to the results for the CFIS light angles, the $\Delta\Sigma_1^{(+)}$ and $f\Delta\Sigma$ estimators yield significant measurements of halo ellipticity. However, the other estimators yield results consistent with zero.

We can repeat the process used for the CFIS angles and calculate the mean halo ellipticity and χ^2 of the fit. The mean halo ellipticity is $e = 0.153 \pm 0.101$ and $\chi^2_\nu = 0.85$. The mean ellipticity from the SDSS light angles is lower than for the CFIS light angles. This is not surprising. As mentioned before, the imaging from SDSS is shallower than it is for CFIS, so we expect the position angles to be less accurate. This could lead to a higher degree of misalignment which would yield a rounder stacked shear.
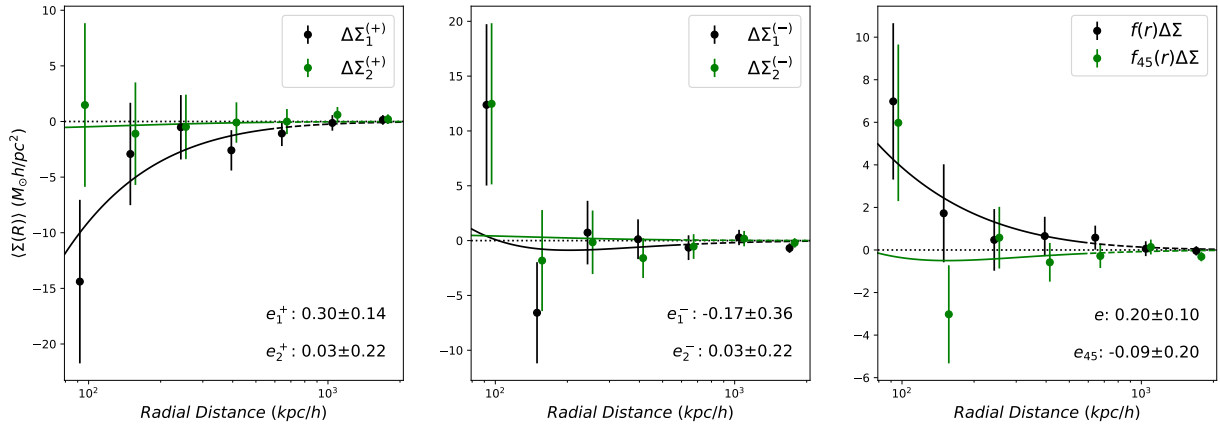
Figure 4.11: Results for quadrupole shear presented in the same format as Figure 4.2. The lens position angle from SDSS was used, as opposed to the lens position angle from CFIS.
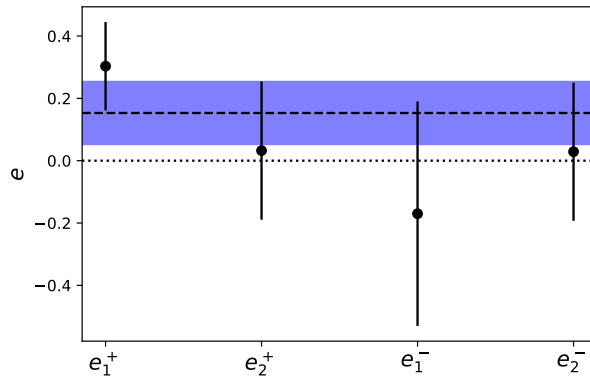

Figure 4.12: Halo ellipticity values calculated using the SDSS light angles. Results are presented in the same format as Figure 4.3.
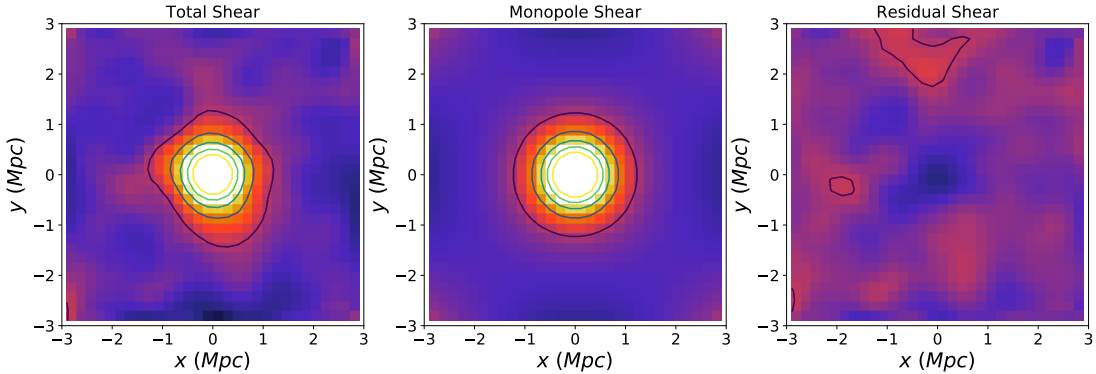
Figure 4.13: Convergence map generated using angles from SDSS. Left: observed convergence. Centre: monopole fit. Right: residual convergence.

The misalignment between the CFIS major axis and the SDSS major axis will obey some probability distribution, which describes how likely the two axes will be separated by a given misalignment angle. As discussed in Section 3.3, this probability distribution can be represented as a double-peaked Gaussian centred on 0 and π. Stacking elliptical haloes with this misalignment probability distribution will yield an effective ellipticity of $e_{eff} = e \cdot \exp(-2\sigma^2)$. If our SDSS light angles are misaligned, they will yield a lower e_{eff} than the ellipticity we measure from the CFIS light angles, e. We can determine the width of the Gaussian distribution. This yields a typical misalignment angle of 25.3°. We can compare this to the standard deviation of the differences between the CFIS angles and SDSS angles from Figure 2.5, which is 33.6°.

The process of creating a convergence map was repeated and the results are shown in Figure 4.13. This figure follows the same format as Figure 4.4. As we saw for the CFIS angles, there is no clear ellipticity in the mass distribution on the left. Once again, this could be due to more noise in the weighted average in each bin as well as the lack of systematic corrections applied to the convergence map.

After analysing the lensing signal around 146,000 LRGs, we have obtained a significant detection of dark matter halo ellipticity. The lenses were aligned with the major axis of the galaxy light from CFIS and stacked to measure the quadrupole shear. The quadrupole shear around 1.5 million randomly oriented lenses was also calculated, and subtracted from the quadrupole estimators in order to account for systematic effects. Two sets of estimators, CJ and NR, were fit to the results to obtain 6 measurements of ellipticity. The results from the CJ estimators are confirmed by the NR estimators. The 4 CJ estimators provide independent measurements of ellipticity. So a mean halo ellipticity and a reduced

55

χ^2 can be calculated. For the CFIS light angles, this is $e = 0.226 \pm 0.102$ and $\chi^2_\nu = 0.62$, indicating a good fit to the 4 measurements by a constant. This was repeated using the SDSS light angles which yielded $e = 0.153 \pm 0.101$ and $\chi^2_\nu = 0.85$. The lower value of halo ellipticity might be expected, as SDSS imaging is shallower than CFIS imaging. This could lead to less accurate position angles and therefore a rounder shear signal when stacking.

Chapter 5

Discussion

In this chapter, we will first discuss satellite galaxies and their role as a potential source of contamination in our measurement of halo ellipticity. Then, we discuss measurements of the quadrupole estimators when aligning with filaments, rather than with lens light. This is done using the angles between the LRG pair axis and lines of constant declination, as discussed in Section 2.2.3. Finally, we will compare our results with results from previous studies.

5.1 Satellite Galaxies

There is no redshift information for sources from CFIS. As a result, we have no way of knowing which sources are actually behind the lens and therefore which are affected by weak lensing. Some portion of the sources surrounding the lenses are actually satellite galaxies. These satellite galaxies are not affected by lensing, and may introduce bias in the form of coherent intrinsic alignment. In this section, we will address this concern and attempt to quantify the effect of satellite galaxies on our measurement of halo ellipticity.

Previously, in Section 2.3, we discussed the azimuthal distribution of sources around the lenses. Specifically, that an excess of sources along the lens major axis and a deficit along the minor axis suggests a portion of the source sample are actually satellite galaxies. This alignment between the satellite distribution and the alignment of the central galaxy has been observed by Yang et al. (2006), who observed a stronger alignment for red central galaxies. Our lenses, being LRGs, are therefore expected to be significantly aligned with their satellite populations. When aligning with the CFIS angles, the amplitude of this non-uniform source distribution was 1.5 $\pm$ 0.3 %. For the SDSS angles it was 1.1 $\pm$ 0.4 %.

There was no significant deviation from a uniform source distribution when aligning with the LRG pairs.

Light from the lens will contaminate the shape measurements of the plentiful sources along the lens major axis. This can lead to the shape measurement being biased in the radial direction (Sifón et al., 2018). In addition to this source of contamination, there is also contamination due to intrinsic alignment of the satellite galaxies. Schneider & Bridle (2010) propose a model for intrinsic alignments of galaxies. Their model is based on the linear alignment model, which assumes the alignment of galaxies is linearly proportional to the tidal field. This model predicts preferential radial alignment of satellites with the central galaxy. However, observational studies have found mixed results. Several studies of satellite alignment yield results consistent with random alignment (Sifón et al., 2015; Schneider et al., 2013), although preferential radial alignment has been observed in others (Singh et al., 2015; Georgiou et al., 2019). If there is a significant preferential radial alignment, an excess of satellites along the major axis will lead to a larger negative contribution near the major axis. This will have the effect of adding a negative quadrupole term, or a negative halo ellipticity, to our results.

We can attempt to quantify how much of an effect we could expect these satellite galaxies to have on our measured halo ellipticity. When aligning with CFIS angles, approximately 1.5% of sources follow a $\cos(2\theta)$ distribution. Presumably the amount of sources that are satellites is actually much higher. However, most of them will bias the monopole. Only the portion that are distributed with $\cos(2\theta)$ dependence will negatively bias our ellipticity.

Georgiou et al. (2019) observed a radial dependence for the amount of contamination due to satellite galaxies. Although this effect is only significant within $\sim 0.3R_{200}$ from the centre of the lens. From the monopole fit, we know that our sample of lenses have an average halo mass of $M_{200} = 1.26 \times 10^{13}\mathrm{M}_\odot$. A halo of this mass will have a virial radius of $R_{200} = 280\,\mathrm{kpc/h}$. Therefore, only galaxies within 84 kpc/h will experience a significant radial alignment. This radial alignment varies depending on the distance between the lens and the source. Satellite galaxies at $0.2R_{200}$, or 56 kpc/h, will experience a mean radial shear of $\langle e_+ \rangle = 0.015$ (Georgiou et al., 2019). However, only sources that are further than 70 kpc/h from their lens galaxies are included in our weighted averages. Satellite galaxies at $0.3R_{200}$, or 84 kpc/h, will experience a mean radial shear of $\langle e_+ \rangle = 0.005$. Any satellites beyond this radius will not experience a significant radial bias.

We can examine how susceptible our measurements of halo ellipticity are to this radial bias. We assume satellites in the innermost radial bin of the quadrupole estimator will experience a radial bias of $\langle e_+ \rangle = 0.005$. In order to calculate how this will affect the
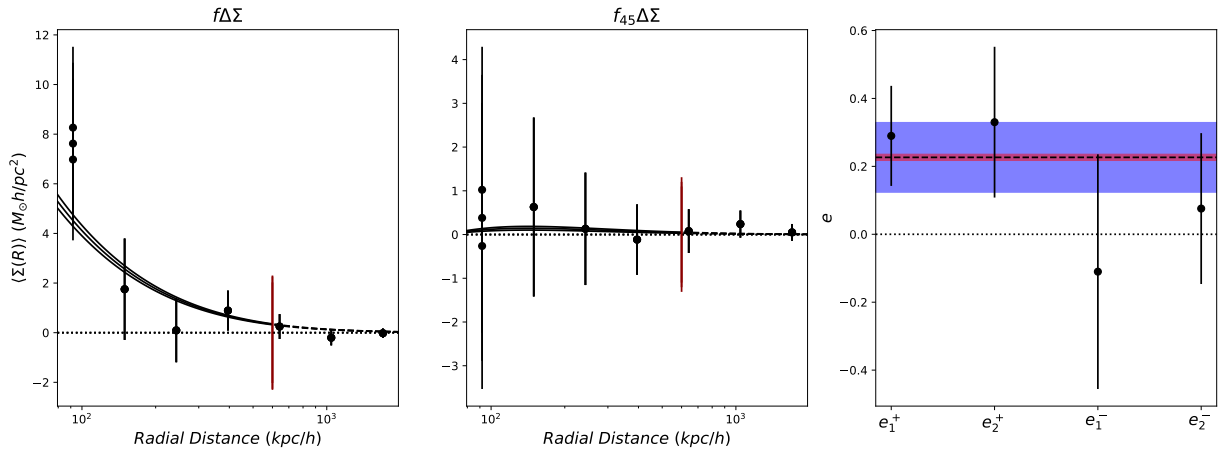
58

Figure 5.1: Results for quadrupole shear after applying bias due to satellite galaxies. NR estimators are displayed in the left and centre subplots. The inner bin has been changed by ± 0.64 M$_\odot$h pc^2 and the fit has been repeated. On the right are the results of calculating mean ellipticity using the CJ estimators. A red band has been added to represent how much the mean ellipticity changes due to contamination from satellite galaxies.

mass density we can use $\Delta\Sigma(r) = \Sigma_{crit}\gamma(r)$. Our lenses will each have a different Σ_{crit} depending on their redshift. After calculating the critical density for each lens, the median is $\Sigma_{crit} = 8566$ M$_\odot$h pc^2. If 1.5% of our sources contribute a radial quadrupole shear, this will lead to a change in the mass density of at most $\Delta\Sigma = 0.64$ M$_\odot$h pc^2 in the innermost bin. There will be no significant change in the mass density in any of the other bins.

If we change the innermost bin of each quadrupole estimator by 0.64 M$_\odot$h pc^2, we can estimate how susceptible the mean halo ellipticity is to this negative quadrupole effect. The negative quadrupole effect will manifest as excess radial shear along the major axis of the lens and excess tangential shear along the minor axis. This will affect each of the estimators in a different way. Examining how the mean halo ellipticity changes, if all estimators are affected, will give us a conservative estimate of how sensitive our results are to contamination from satellite galaxies.

Figure 5.1 displays results after applying a bias due to satellite galaxies. The NR estimators are displayed in the left and centre subplots. The inner bin has been changed by ± 0.64 M$_\odot$h pc^2 and the fit has been repeated. The right subplot displays the results of calculating the mean halo ellipticity using the CJ estimators. The format is the same as previous mean ellipticity plots, but a red band has been added to represent how much the mean ellipticity changes due to contamination from satellites galaxies. This effect yields an

upper limit of $e = 0.235$ and a lower limit of $e = 0.217$ compared to our mean halo ellipticity of $e = 0.226 \pm 0.102$. Even a conservative estimate of the effects of contamination from satellite galaxies yields results well within the 1σ range of uncertainty of the mean halo ellipticity. This suggests contamination from satellite galaxies does not have a significant effect on our results.

5.2   LRG Pairs

When aligning and stacking the quadrupole shear, we have made the assumption that the light of the galaxy is aligned with the dark matter halo. If this is not true it would lead to stacking misaligned dark matter haloes, which could cause the halo ellipticity to be underestimated. Aligning along the filaments in which the LRGs reside offers an alternative method of measuring the halo ellipticity. We can detect these filaments by grouping the LRGs into pairs. As we discussed in Section 2.2.3, this was done by limiting pairs to a redshift separation of $\Delta z = 0.002$ and a projected separation range of $6 - 10$ Mpc/h.

We expect there to be a correlation between the major axis of the LRG light and the angle to its partner. The LRG pairs are expected to reside along filaments of dark matter within the greater cosmic web. When these haloes and their resident galaxies form, they will be affected by the gravitational pull of the surrounding large-scale structure. This will cause the galaxy and the dark matter halo to become preferentially aligned along the filament. This alignment has been observed for galaxy light in observations (Georgiou et al., 2019). Simulations by Ganeshaiah Veena et al. (2019) have also revealed a preferential alignment between dark matter haloes and filaments. It is thought that galaxies acquire their alignment from the surrounding structure early on, when they are still forming. The orientations of haloes are affected by the ongoing process of accretion and mergers, causing them to maintain their alignment with the filaments.

In Section 2.3, we studied the azimuthal distribution of sources around the lens galaxies. We expect the dark matter halo to be aligned with the satellite galaxy distribution, corresponding to a quadrupole $\cos(2\theta)$ dependence in the number of sources around the lens. We saw a significant amplitude in the quadrupole of the distribution of sources when aligning with the angle of the LRG light, suggesting the lens galaxy light is aligned with its satellite distribution and presumably its halo. However, we did not see a significant alignment of the source galaxies when aligning with the filament. This suggests that the halo may be poorly aligned with the filaments, and that aligning with the LRG light may be a better way to observe the halo ellipticity. If this is true, we expect to see less significant measurements of halo ellipticity from the quadrupole estimators.
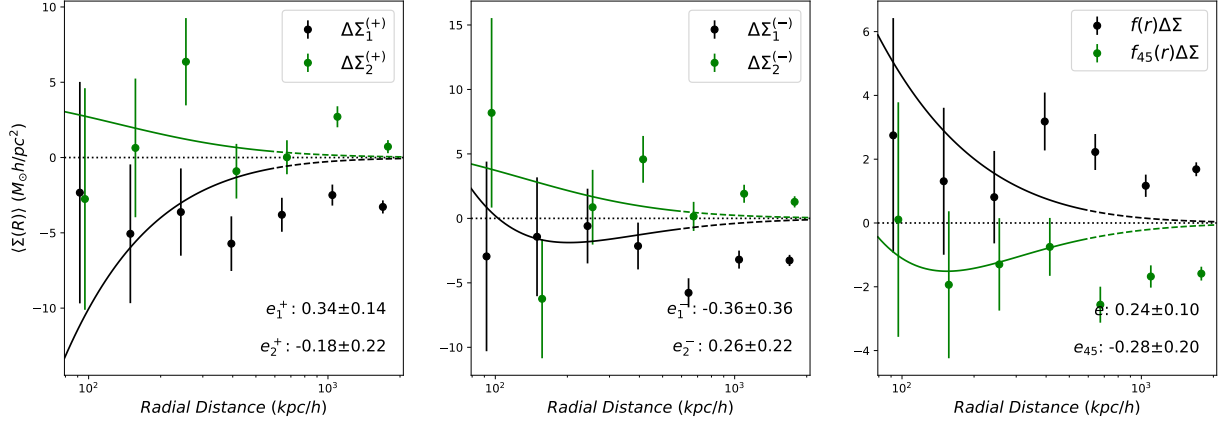
Figure 5.2: Results for quadrupole shear presented in the same format as Figure 4.2. Rather that rotating by the angle of the galaxy light, the angle to the LRG pair counterpart was used. We do not expect the model to be a good fit.

Rather than aligning to a new coordinate system where the x-axis is aligned with the major axis of the LRG light, we now rotate to a coordinate system where the x-axis is aligned with the LRG pair. The process of calculating the quadrupole shear is the same as it was for the LRG light angles. Results using these pair angles are visible in Figure 5.2. The same multipole model was fit to the data in order to obtain a value of ellipticity from each estimator. However, we expect our model of a monopole and a quadrupole term is no longer adequate. This model was designed to describe an *isolated* elliptical halo, but the anisotropic lensing signal will extend much further when aligning with the filaments. The model would need to be developed further, possibly by the addition of higher order terms in the multipole, in order to account for the lensing signal from the filament. This expansion of the model was not undertaken and is left for a future work.

As expected, the results for the quadrupole shear appear quite different from how they appear in Figure 4.2 for the angles of the light. The model was not designed to account for anisotropy at large radii, as we would expect along a filament as opposed to an isolated galaxy. We can see from each of the fits that there are several points which are separated by many standard deviations from the fit. Therefore, the values of halo ellipticity from the fits are not meaningful.

Ellipticity measurements and mean halo ellipticity for pair angles are displayed in Figure 5.3. The mean halo ellipticity is $e = 0.157 \pm 0.101$ and $\chi^2_\nu = 2.10$. As we expected, the high value of χ^2_ν suggests the model is not well suited for the observations. The model was not designed to describe the anisotropy of filaments, so the mean halo ellipticity is not
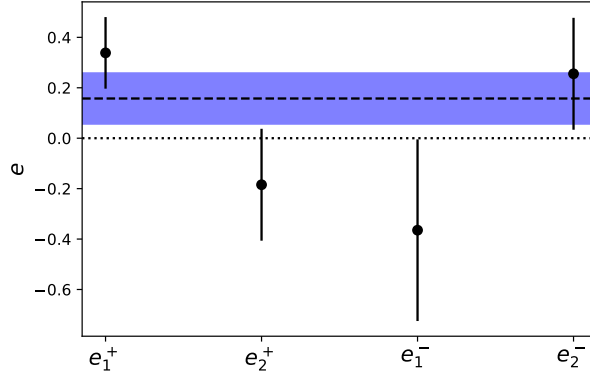
61

Figure 5.3: Halo ellipticity measurements and mean halo ellipticity using LRG pair angles. Results are presented in the same format as Figure 4.3.

meaningful.

A κ map was produced after alignment with the position angles for pairs, rather than the position angles of the light. Results are displayed in Figure 5.4. This figure follows the same format as Figure 4.4. As we saw for the light angles from CFIS and SDSS, there is no evidence of an elliptical mass distribution.

Aligning our coordinate system with the filaments offers an alternative to aligning with the lens light. We can see from Figure 5.2 that the quadrupole estimators appear quite different from how they behaved when aligning with the light in Figure 4.2. Although the models do not appear to be a good fit, the quadrupole estimators behave as expected. The $\Delta\Sigma_1^{(+)}$ estimator is still significantly negative over the radial range, while the $f\Delta\Sigma$ estimator is still significantly positive. These estimators both indicate the presence of excess tangential shear along the major axis and excess radial shear along the minor axis. However, the estimators evolve differently with radius than for an isolated halo. Although we expect the anisotropy of the dark matter halo to only extend out to R_{200}, the filament will extend much further. This filament will also contribute an anisotropic signal to our measurement, especially at large distances from the lens. The addition of higher order terms to the multipole expansion may allow us to account for anisotropic lensing from the filament.
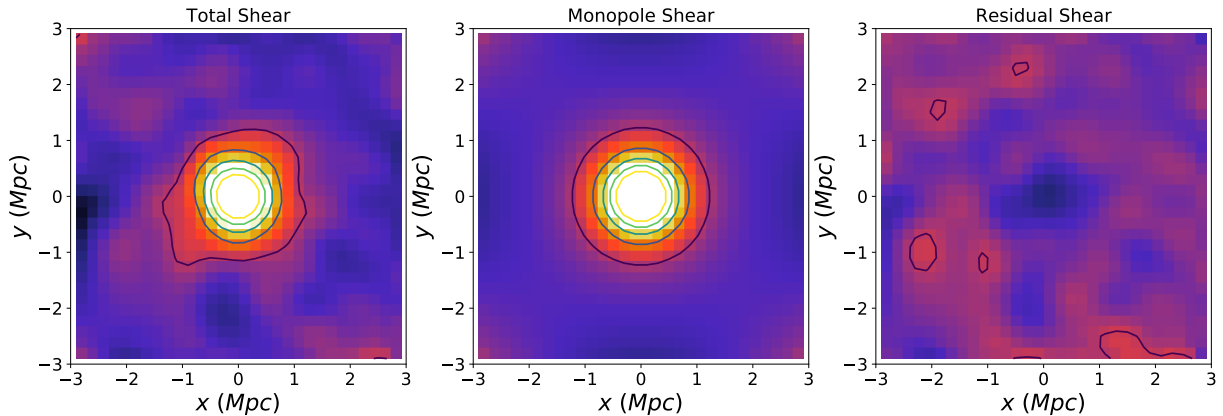
Figure 5.4: Results of KSB on the shear map using LRG pair angles. On the left is the convergence from the data after correcting the inner bins. In the centre is the result of the monopole fit. On the right are the results from the residuals after subtracting the monopole shear.

5.3 Comparison to Previous Results

In order to measure the ellipticity of the dark matter halo, we studied the quadrupole shear. This is the azimuthal variation of the shear with respect to the major axis of the halo. In order to measure this quadrupole shear, while minimising any contribution from the monopole, 6 quadrupole estimators were utilised. Two sets of independent estimators were used: 4 CJ estimators, which are the main focus of this work, and 2 NR estimators, which serve to confirm the results of the CJ estimators. Both sets of estimators indicate significant halo ellipticity. The 4 CJ estimators provide independent measurements of the halo ellipticity, and taking a weighted average of these 4 estimators will yield a mean halo ellipticity. When aligning with the CFIS light angles, this mean halo ellipticity is $e = 0.226 \pm 0.102$ after correcting for systematics. When aligning with the SDSS light angles instead, the mean halo ellipticity is $e = 0.153 \pm 0.101$.

This is in agreement with results from N-body simulations. Simulations by Dubinski & Carlberg (1991) found the distribution of projected ellipticities peaks at $e = 0.5$, however the haloes become rounder when measured at larger radii. A limit of 100 kpc was imposed on their measurements of halo ellipticity, which is well within the virial radius of their haloes. Our measurements of halo ellipticity extend further, beyond the virial radius for our haloes, so it is not surprising that our haloes are observed to be rounder. Simulations are also unburdened by complications arising from light-halo misalignment, which may

63

cause weak lensing observations to underestimate the ellipticity (see Section 3.3). Other simulations are in better agreement with our results. Warren et al. (1992) study a larger number of haloes in several different simulations. They observe a trend of decreasing ellipticity when studying the ellipticity distribution in several radial bins. The peak of the ellipticity distributions tend to $e = 0.25$ beyond 50 kpc. Bailin & Steinmetz (2005) explore the ellipticity of dark matter haloes at lower masses in simulations and observe a mean projected ellipticity of $e = 0.24$.

Our results are also in good agreement with other results from weak lensing. Parker et al. (2007) study halo ellipticity using weak galaxy-galaxy lensing and measure an ellipticity of ~ 3 at the 2σ level. Clampitt & Jain (2016) study halo ellipticity using the CJ estimators and SDSS LRGs. The best fit to all 4 CJ estimators is a halo ellipticity of $e = 0.24 \pm 0.06$. Results for the redMaPPer clusters yielded similar results, with an ellipticity of $e = 0.21$.

Hoekstra et al. (2004) measure a halo ellipticity of $e = 0.33^{+0.07}_{-0.09}$. This is more elliptical than our mean halo ellipticity. However, their lenses are more elliptical than ours. The average ellipticity of their lens sample is $\langle e \rangle = 0.414$, while the median ellipticity of our lenses is $e = 0.111$. Their model assumes that halo ellipticity is related to the ellipticity of the light through a factor f. As a result, the high mean ellipticity of their lenses led to a high halo ellipticity. In fact, many of the galaxies in their sample are likely spirals viewed edge-on, which would appear as highly elliptical galaxies. This could explain their high mean ellipticity. Their higher value of halo ellipticity could also suggest that more elliptical galaxies are more likely to reside within more elliptical haloes.

A similar multipole lensing distribution was used by van Uitert et al. (2017) to study elliptical dark matter haloes. Their haloes had an average halo mass of $M_{200} = 1.50^{+0.25}_{-0.24} \times 10^{13} M_{\odot}$, which is similar to the mass of our LRGs. They orient along the major axis of the BCG light and measure the quadrupole shear. Within a range of $40 - 250$ kpc they obtain a best fit halo ellipticity of $e = 0.38 \pm 0.12$. However, they perform this fit over multiple radial ranges. As the range of the fit increases to larger radii, the fit ellipticity decreases. They also fit over a range of $40 - 750$ kpc, which is much more similar to our fit range, and obtain a halo ellipticity of $e = 0.24 \pm 0.08$. This is in much better agreement with our halo ellipticity.

In addition to measuring halo ellipticity, we also studied satellite distributions in order to motive our choice of alignment angle. When aligning with the major axis of the light and counting the number of sources in angular bins, we observe a significant quadrupole dependence in the source distribution. The amplitude of this $\cos(2\theta)$ dependence is $1.5 \pm 0.3\%$. This is evidence for the inclusion of satellites in our source sample.

Yang et al. (2006) studied several groups from SDSS. They divided the area around the central galaxies into angular bins and counted the number of satellites in each bin. They calculate the normalized pair count for each angular bin $f_{pairs}(\theta) = N(\theta)/\langle N_R(\theta)\rangle$, where $N_R(\theta)$ are counts where the central galaxy major axis angle has been randomized. In the angular bin along the major axis, $f_{pairs} \sim 1.2$, which can also be thought of as a $\sim 20\%$ quadrupole dependence in order to compare with our quadrupole amplitude. Most of our sources are not satellites, and it is not possible to separate the background sources from genuine satellites. As a result our amplitude is much smaller. We also observe a radial dependence, with the amplitude decreasing as radius increases and the possibility of finding satellites becoming increasingly unlikely.

We also studied the distribution of source galaxies when aligning along the filaments. Ganeshaiah Veena et al. (2019) studied the alignment of DM haloes with respect to filaments in simulations. Their simulations reveal a preferential alignment between halo major axis and the filaments. This correlation is largely mass independent and more prominent for ellipticals than for spirals. Knowing this, it is interesting that the azimuthal source distribution did not exhibit a significant quadrupole when aligned with the filaments. A fit of $\cos(2\theta)$ to the counts in angular bins yields an amplitude of $0.3 \pm 0.2\%$. Simulations by Bailin & Steinmetz (2005) also show preferential major axis alignment along filaments. However, the correlation falls off with distance. They note the alignments are stronger for group and cluster mass haloes. Previous studies, which focus on the shapes and alignments of these massive haloes, may overestimate these correlations.

Chapter 6

Conclusion

In this thesis, we present a method of measuring dark matter halo ellipticity using weak gravitational lensing. We present the methodology required to measure the quadrupole shear. We develop a model to describe the mass distribution of the dark matter halo. We apply this model and utilize two sets of estimators to measure the quadrupole shear. The quadrupole estimators provide independent measurements of halo ellipticity that allow us to calculate a mean halo ellipticity.

We investigated different methods of aligning the coordinate system when stacking the shear. Our primary method of aligning with the major axis of the lens galaxy light is justified by the detection of quadrupole dependence in the azimuthal source distribution around the lenses. This quadrupole dependence is significant, with an amplitude of $1.5 \pm 0.3\%$ when aligning the coordinate system with the major axis of the galaxy light. The quadrupole dependence corresponds to the satellite galaxies, which are a useful tracer of the host dark matter halo.

We studied the lensing signal around 146,000 LRGs from BOSS with sources from CFIS. Fitting an NFW profile to the monopole shear profile yields an average mass of $M_{200} = 1.26 \pm 0.07 \times 10^{13}$ $M_{\odot}$ and a concentration of $c_{200} = 2.01 \pm 0.22$. After fitting the monopole, we fit 6 estimators to the quadrupole shear to obtain 6 measurements of halo ellipticity. When aligning our coordinate system with the major axis of the lens light, we measure a mean halo ellipticity of $e = 0.226 \pm 0.102$ for CFIS light angles and $e = 0.153 \pm 0.101$ for SDSS light angles. This value is in agreement with other measurements of halo ellipticity from weak lensing (Clampitt & Jain, 2016; van Uitert et al., 2017). We also present a method of measuring the quadrupole shear when aligning along filaments rather than along the major axis of the light. Although our model is not well suited to

describe the anisotropic shear at large distances that are expected near filaments, we were able to observe significant quadrupole shear. In order to adequately describe the shear experienced near a filament, the model needs to be developed further.

The major axis of the satellite distribution, rather than the major axis of the light or the filament, is an interesting choice of alignment for future studies. Due to their role as dynamical tracers, the satellite distribution is potentially less prone to misalignment with the halo than the light. Measurements of halo ellipticity for cluster mass haloes have been performed using satellite distributions (Gonzalez et al., 2020). This has been extended down to group scales by van Uitert et al. (2017), who found the satellite distribution to be a better proxy than the orientation of the lens light on larger scales. Applying this alignment proxy will require photometric redshifts for the sources in order to identify which are satellites.

Prospects for improving halo ellipticity measurements are promising. CFIS is still underway, with plans to cover 5000 square degrees which compliment existing spectroscopy from SDSS. An increase in the source sample of this size could potentially decrease the uncertainty by a factor of 1.6, changing the 1σ uncertainty in the mean halo ellipticity from ± 0.101 to $\sim \pm 0.063$. CFIS also plans to complete multi-band imaging, which will allow for the calculation of photometric redshifts. Other upcoming surveys are expected to include a large number of objects, which would provide more lenses and sources for weak lensing. The recently completed Dark Energy Survey (DES: The Dark Energy Survey Collaboration, 2005) covers 5000 square degrees in four bands of imaging, which will provide photometric redshifts, and shapes for approximately 200 million galaxies. Photometric redshifts for sources will further improve our results, enabling us to remove contamination from satellite galaxies and more accurately calculate the critical density. However, there is no SDSS spectroscopy in the area covered by DES. The SDSS-IV Extended Baryon Oscillation Spectroscopic Survey (eBOSS: Dawson et al., 2016) will contribute 250,000 new spectroscopically confirmed LRGs within a redshift range of $0.6 < z < 1.0$, which will greatly expand the lens sample. Large-scale space based observations are not susceptible to the same limitation of ground based observations. These surveys will be free of contamination from the atmosphere, greatly reducing the effect of the PSF on shape measurements. Euclid (Laureijs et al., 2011) and WFIRST (Spergel et al., 2015) are two upcoming missions that promise to provide a large area of space based imaging, enabling more accurate shape measurements. We expect measurements of halo ellipticity from weak lensing to continue to improve in the future.

References

Adhikari S., Chue C. Y. R., Dalal N., 2015, JCAP, 2015, 009

Allgood B., Flores R. A., Primack J. R., Kravtsov A. V., Wechsler R. H., Faltenbacher A., Bullock J. S., 2006, MNRAS, 367, 1781

Aragón-Calvo M. A., van de Weygaert R., Jones B. J. T., van der Hulst J. M., 2007, ApJL, 655, L5

Azzaro M., Patiri S. G., Prada F., Zentner A. R., 2007, MNRAS, 376, L43

Bailin J., Steinmetz M., 2005, ApJ, 627, 647

Baltz E. A., Marshall P., Oguri M., 2009, JCAP, 1, 015

Bartelmann M., Schneider P., 2001, Phys Rep, 340, 291

Bertin E., Arnouts S., 1996, A&AS, 117, 393

Blazek J., McQuinn M., Seljak U., 2011, JCAP, 2011, 010

Brainerd T. G., 2005, ApJL, 628, L101

Brainerd T. G., Blandford R. D., Smail I., 1996, ApJ, 466, 623

Clampitt J., Jain B., 2016, MNRAS, 457, 4135

Clampitt J., Miyatake H., Jain B., Takada M., 2016, MNRAS, 457, 2391

Colberg J. M., Krughoff K. S., Connolly A. J., 2005, MNRAS, 359, 272

Davé R., Spergel D. N., Steinhardt P. J., Wandelt B. D., 2001, ApJ, 547, 574

Dawson K. S., et al., 2013, AJ, 145, 10

Dawson K. S., et al., 2016, AJ, 151, 44

Dubinski J., Carlberg R. G., 1991, ApJ, 378, 496

Duffy A. R., Schaye J., Kay S. T., Dalla Vecchia C., 2008, MNRAS, 390, L64

Dutton A. A., Macciò A. V., 2014, MNRAS, 441, 3359

Eisenstein D. J., et al., 2011, AJ, 142, 72

Epps S. D., Hudson M. J., 2017, MNRAS, 468, 2605

Evans A. K. D., Bridle S., 2009, ApJ, 695, 1446

Ganeshaiah Veena P., Cautun M., Tempel E., van de Weygaert R., Frenk C. S., 2019, MNRAS, 487, 1607

Georgiou C., et al., 2019, A&A, 628, A31

Gillis B. R., et al., 2013, MNRAS, 431, 1439

Gonzalez E. J., Makler M., Garcia Lambas D., Chalela M., Pereira M. E. S., Van Waerbeke L., Shan H., Erben T., 2020, arXiv e-prints, p. arXiv:2006.08651

Hirata C. M., Seljak U., 2004, PhysRevD, 70, 063526

Hirata C. M., Mandelbaum R., Ishak M., Seljak U., Nichol R., Pimbblet K. A., Ross N. P., Wake D., 2007, MNRAS, 381, 1197

Hoekstra H., Yee H. K. C., Gladders M. D., 2004, ApJ, 606, 67

Hudson M. J., Gwyn S. D. J., Dahle H., Kaiser N., 1998, ApJ, 503, 531

Hudson M. J., et al., 2015, MNRAS, 447, 298

Huff E., Mandelbaum R., 2017, arXiv e-prints, p. arXiv:1702.02600

Ibata R., Lewis G. F., Irwin M., Totten E., Quinn T., 2001, ApJ, 551, 294

Jing Y. P., Suto Y., 2002, ApJ, 574, 538

Joachimi B., et al., 2015, SSR, 193, 1

Kaiser N., Squires G., 1993, ApJ, 404, 441

Kaiser N., Squires G., Broadhurst T., 1995, ApJ, 449, 460

Khoury J., 2015, PhysRevD, 91, 024022

Laureijs R., et al., 2011, arXiv e-prints, p. arXiv:1110.3193

Libeskind N. I., Cole S., Frenk C. S., Okamoto T., Jenkins A., 2007, MNRAS, 374, 16

Lima M., Cunha C. E., Oyaizu H., Frieman J., Lin H., Sheldon E. S., 2008, MNRAS, 390, 118

Mandelbaum R., Hirata C. M., Ishak M., Seljak U., Brinkmann J., 2006a, MNRAS, 367, 611

Mandelbaum R., Seljak U., Kauffmann G., Hirata C. M., Brinkmann J., 2006b, MNRAS, 368, 715

Mandelbaum R., Hirata C. M., Broderick T., Seljak U., Brinkmann J., 2006c, MNRAS, 370, 1008

McKay T. A., et al., 2002, ApJL, 571, L85

Milgrom M., 1983, ApJ, 270, 365

Milgrom M., 2013, PhysRevLett, 111, 041105

Miller L., Kitching T. D., Heymans C., Heavens A. F., van Waerbeke L., 2007, MNRAS, 382, 315

Miller L., et al., 2013, MNRAS, 429, 2858

Natarajan P., Refregier A., 2000, ApJL, 538, L113

Navarro J. F., Frenk C. S., White S. D. M., 1997, ApJ, 490, 493

Oguri M., Takada M., Okabe N., Smith G. P., 2010, MNRAS, 405, 2215

Okumura T., Jing Y. P., 2009, ApJL, 694, L83

Okumura T., Jing Y. P., Li C., 2009, ApJ, 694, 214

Parker L. C., Hoekstra H., Hudson M. J., van Waerbeke L., Mellier Y., 2007, ApJ, 669, 21

Peter A. H. G., Rocha M., Bullock J. S., Kaplinghat M., 2013, MNRAS, 430, 105

Prada F., et al., 2003, ApJ, 598, 260

Rykoff E. S., et al., 2014, ApJ, 785, 104

Schneider M. D., Bridle S., 2010, MNRAS, 402, 2127

Schneider M. D., et al., 2013, MNRAS, 433, 2727

Schrabback T., et al., 2015, MNRAS, 454, 1432

Sheldon E., 2015, NGMIX: Gaussian mixture models for 2D images (ascl:1508.008)

Sheldon E. S., et al., 2004, AJ, 127, 2544

Sheldon E. S., et al., 2009, ApJ, 703, 2217

Sifón C., Hoekstra H., Cacciato M., Viola M., Köhlinger F., van der Burg R. F. J., Sand D. J., Graham M. L., 2015, A&A, 575, A48

Sifón C., Herbonnet R., Hoekstra H., van der Burg R. F. J., Viola M., 2018, MNRAS, 478, 1244

Singh S., Mandelbaum R., More S., 2015, MNRAS, 450, 2195

Spergel D., et al., 2015, arXiv e-prints, p. arXiv:1503.03757

The Dark Energy Survey Collaboration 2005, arXiv e-prints, pp astro–ph/0510346

Vera-Ciro C., Helmi A., 2013, ApJL, 773, L4

Viola M., et al., 2015, MNRAS, 452, 3529

Warren M. S., Quinn P. J., Salmon J. K., Zurek W. H., 1992, ApJ, 399, 405

Yang X., van den Bosch F. C., Mo H. J., Mao S., Kang X., Weinmann S. M., Guo Y., Jing Y. P., 2006, MNRAS, 369, 1293

Yang T., Hudson M. J., Afshordi N., 2020, arXiv e-prints, p. arXiv:2001.10943

Zentner A. R., Kravtsov A. V., Gnedin O. Y., Klypin A. A., 2005, ApJ, 629, 219

Zheng Z., Zehavi I., Eisenstein D. J., Weinberg D. H., Jing Y. P., 2009, ApJ, 707, 554

van Haarlem M., van de Weygaert R., 1993, ApJ, 418, 544

van Uitert E., et al., 2017, MNRAS, 467, 4131

APPENDICES

Appendix A

Offset Group Term

Often lens galaxies in our stack will be satellite galaxies within a larger host halo. The offset group term describes the contribution to the lensing signal from the host halo. Gillis et al. (2013) represent the offset group term as a convolution.

$$\Delta\Sigma_{OG} = \int_0^\infty \Delta\Sigma_{host}(R, R_s)P(R_s)dR_s \tag{A.1}$$

The $\Delta\Sigma_{host}(R, R_s)$ term is the value of the host NFW profile at a distance of R from the centre of the satellite halo. The satellite halo is distance R_s from the centre of the host halo. The probability function $P(R_s)$ describes how likely one is to find a satellite halo at a given R_s from the centre of the host halo.

$$P(R_s) = \frac{1}{N}R_s\Sigma(R_s) \tag{A.2}$$

$\Sigma(R_s)$ is the NFW profile density at distance R_s from the centre of the host halo. N is a normalisation factor.

There are several different ways to calculate the offset group term. The most obvious is to perform a numerical integration. This is done by first integrating over angles from 0 to 2π in a ring a certain radius from the centre of the satellite halo. The distance from the centre of the host halo to each point on this ring is calculated using the cosine law. Next, integrate over the radius to the centre of the satellite from the centre of the host halo. Then, integrate over the distance from the centre of the satellite halo. A weighted average is performed using the value of the probability function $P(R)$ at each radius. This yields $\Delta\Sigma_{OG}(R)$.

Although this method is straightforward, it is rather time consuming. We develop two other methods of calculating the offset group term and compare the results. These two methods involve using the 2-dimensional Fourier transform and the Hankel transform.

The 2-dimensional Fourier transform is

$$F(k) = \int_{\infty}^{\infty} f(r)e^{-2\pi i k r} dr \tag{A.3}$$

In practice, a fast Fourier transform (FFT) will be performed. This is a discrete Fourier transform

$$A_k = \sum_{m=0}^{n-1} a_m \exp\left(-2\pi i \frac{mk}{n}\right) \tag{A.4}$$

$$a_m = \frac{1}{n} \sum_{k=0}^{n-1} A_k \exp\left(2\pi i \frac{mk}{n}\right) \tag{A.5}$$

For two dimensions, this becomes

$$A_{kl} = \sum_{m=0}^{M-1} \sum_{n=0}^{N-1} a_{mn} \exp\left[-2\pi i \left(\frac{mk}{M} + \frac{nl}{N}\right)\right] \tag{A.6}$$

To perform the convolution, a $6000\,\mathrm{kpc} \times 6000\,\mathrm{kpc}$ grid was created. Each cell in the grid is $10\,\mathrm{kpc} \times 10\,\mathrm{kpc}$ and the grid runs from -3000 kpc to 3000 kpc. The distance from the centre of the grid was calculated at each point.

$$d(x,y) = \sqrt{x^2 + y^2} \tag{A.7}$$

$\Delta\Sigma_{NFW}(R)$ for a halo of mass M_{group} is calculated at each point in the grid using Equation 3.19. The probability $P(R)$ is also calculated for each point. The probability function is different in this case because we are performing a two dimensional Fourier transform. We remove the factor of R from the probability function that is required in the one dimensional case. Now the probability function is

$$P(R) = \frac{1}{M_{proj}(R_{200})} \Sigma_{NFW}(R) \tag{A.8}$$

where M_{proj} is calculated using Equation 3.20 and $\Sigma_{NFW}(R)$ is calculated using Equation 3.15. The NFW profile goes to infinity at the very centre, so the central cell in each of these two grids was instead set as the mean of the four directly adjacent cells. Now we can use the convolution theorem to calculate the offset group term.

$$f * g = \mathcal{F}^{-1}(\mathcal{F}(f) \cdot \mathcal{F}(g)) \tag{A.9}$$

74

The 2D FFT of each grid is calculated using Equation A.4. These two transformed grids are multiplied and the inverse 2D FFT is applied using Equation A.5.

Rather than using the Fourier transform to perform the convolution, we can use the Hankel transform.

$$F_\nu(k) = \int_0^\infty f(r)J_\nu(kr)rdr \tag{A.10}$$

This is related to the circularly symmetric form of the Fourier transform.

$$F(k) = \int \int f(r)e^{ik\cdot r}dr = 2\pi \int_0^\infty f(r)J_0(kr)rdr \tag{A.11}$$

$$f(r) = \frac{1}{2\pi} \int_0^\infty F(k)J_0(kr)kdk \tag{A.12}$$

By making use of the `hankel` package in Python, we can compare the Hankel convolution to the 2D FFT convolution. This package allows the user to create a Hankel transformation object. The user can specify the number of steps in the integration (N) and the step size in the integration (h). Often, the result will be sensitive to the choice of these parameters. As we did in the 2D Fourier convolution, we will also be using Equation A.8 as the probability function for the Hankel convolution. The additional factor of R that was initially included is unnecessary in two dimensions.

Before comparing the results of the convolutions, we may first wish to compare the results of the Hankel transform with the results from the Fourier transform. In order to directly compare the transformed function, we need to make a few changes to our Hankel transform. In Equation A.11, there is a missing factor of 2π that is present in the Fourier transform in Equation A.3. We wish to compare the same k-range, so we will multiply the k-range we used to calculate the Fourier transform by 2π. There is an additional factor of 2π in from of the Hankel transform in Equation A.11 when comparing the Hankel and Fourier transforms. So we also need to multiply the resulting transformed function by 2π. After performing the transformation, we need to divide k by 2π before plotting the Hankel transform to make sure it agrees with the Fourier transform.

We can use the *hankel* package in python to transform and inverse transform functions. There are three parameters that must be adjusted to recover accurate transformations and inverse transformations. The first is a range of k values for the transformed function. These will be used to generate a spline to interpolate points for the inverse transformation. It is important that the lowest range of k values is well sampled to accurately describe the behaviour at the upper end of the $\Delta\Sigma_{NFW}$ profile. The other two important parameters
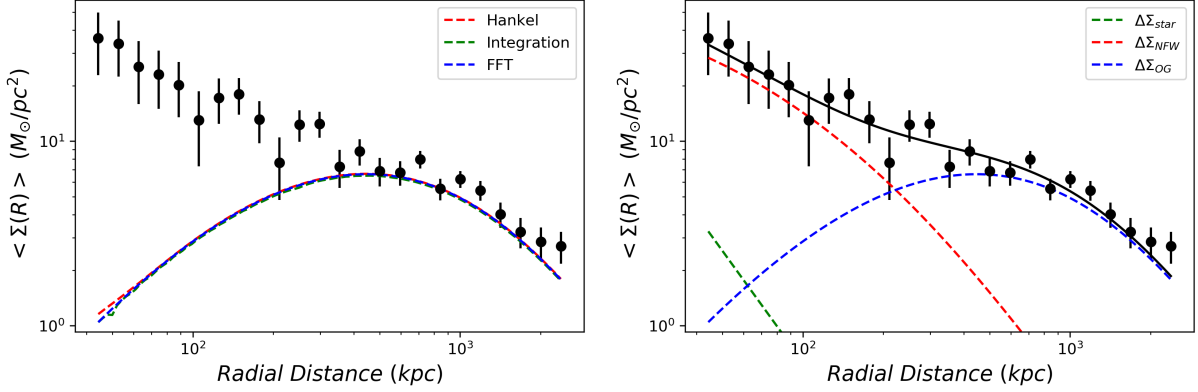
Figure A.1: Left: Comparison of the three different methods for calculating the offset group term. The numerical integration method is in green, the FFT method is in blue, and the Hankel transform method is in red. The three methods are in good agreement. Right: The model with all terms present. The one-halo stellar mass term is in green, the one-halo dark matter term is in red, and the offset group term is in blue.

are the number of integration steps, N, and the step size, h. These can be relatively low for a $\Delta\Sigma_{NFW}$ profile.

Convolving using the FFT or the Hankel transform yields the $\Sigma_{OG}(R)$ profile.

$$\Sigma_{OG}(R) = \int_0^\infty \Sigma_{NFW}(R)P(R)dR \qquad (A.13)$$

Rather than calculating $\Delta\Sigma_{OG}$ from the convolution, we instead calculate it using

$$\Delta\Sigma_{OG}(R) = \left(2\pi \int_0^R \Sigma_{OG}(R')R'dR'\right)\frac{1}{\pi R^2} - \Sigma(R) \qquad (A.14)$$

The three methods are compared on the left in Figure A.1. The numerical integration method is in green, the FFT method is in blue, and the Hankel transform method is in red. The three methods are in good agreement. The right side of this figure displays the model with all terms present. The one-halo stellar mass term is in green, the one-halo dark matter term is in red, and the offset group term is in blue.

Calculating the offset group term is different in an anisotropic system. For a function that can be expressed as a multipole expansion, like our mass distribution,

$$f(r,\theta) = \sum f_m(r)e^{im\theta} \qquad (A.15)$$

76

the Hankel transform becomes

$$F(k) = 2\pi \sum_m i^m e^{im\theta_k} \int_0^\infty f_m(r) J_m(kr) r dr \tag{A.16}$$

To calculate the offset group term, we still convolve the mass density with a probability function. Now both of these functions are 2D and anisotropic, but the method is similar. First, Hankel transform $\Sigma(r, \theta)$ and $P(r, \theta)$.

$$F_\Sigma(k) = \int_0^\infty \Sigma_0(r) J_0(kr) r dr - \cos(2\theta) \int_0^\infty \Sigma_2(r) J_2(kr) r dr \tag{A.17}$$

$$F_P(k) = \int_0^\infty P_0(r) J_0(kr) r dr - \cos(2\theta) \int_0^\infty P_2(r) J_2(kr) r dr \tag{A.18}$$

Then we multiply the transformed functions.

$$
\begin{aligned}
F_\Sigma(k) \cdot F_P(k) &= \int_0^\infty \Sigma_0(r) J_0(kr) r dr \int_0^\infty P_0(r) J_0(kr) r dr \\
&+ \int_0^\infty \Sigma_0(r) J_0(kr) r dr \int_0^\infty P_2(r) J_2(kr) r dr + \int_0^\infty \Sigma_2(r) J_2(kr) r dr \int_0^\infty P_0(r) J_0(kr) r dr \\
&+ \int_0^\infty \Sigma_2(r) J_2(kr) r dr \int_0^\infty P_2(r) J_2(kr) r dr \\
&= F_0(k) + F_2(k) + F_4(k)
\end{aligned}
\tag{A.19}
$$

Which leaves us with three terms. We then apply the inverse Hankel transform to each term according to its index, m.

$$f_m(r) = \frac{1}{2\pi} \int_0^\infty F_m(k) J_m(kr) k dk \tag{A.20}$$

This gives us a monopole, a quadrupole, and an octupole term.

$$\Sigma_{OG}(r, \theta) = \Sigma_{OG,0} + \Sigma_{OG,2} \cos(2\theta) + \Sigma_{OG,4} \cos^2(2\theta) \tag{A.21}$$

Results obtained using this method agree with results from the 2D FFT method, which is unchanged even after introducing anisotropy.